Origins of Chemical Diversity of Back-Arc Basin Basalts: A Segment-Scale Study of the Eastern Lau Spreading Center

Origins of chemical diversity of back-arc basin basalts: A segment-scale study of the Eastern Lau Spreading Center

Antoine Bézos,[1,2] Stéphane Escrig,[1] Charles H. Langmuir,[1] Peter J. Michael,[3] and Paul D. Asimow[4]

Received 10 July 2008; revised 24 January 2009; accepted 6 April 2009; published 30 June 2009.

[1] We report major, trace, and volatile element data on basaltic glasses from the northernmost segment of the Eastern Lau Spreading Center (ELSC1) in the Lau back-arc basin to further test and constrain models of back-arc volcanism. The zero-age samples come from 47 precisely collected stations from an 85 km length spreading center. The chemical data covary similarly to other back-arc systems but with tighter correlations and well-developed spatial systematics. We confirm a correlation between volatile content and apparent extent of melting of the mantle source but also show that the data cannot be reproduced by the model of isobaric addition of water that has been broadly applied to back-arc basins. The new data also confirm that there is no relationship between mantle temperature and the wet melting productivity. Two distinct magmatic provinces can be identified along the ELSC1 axis, a southern province influenced by a "wet component" with strong affinities to arc volcanism and a northern province influenced by a "damp component" intermediate between enriched mid-ocean ridge basalts (E-MORB) and arc basalts. High–field strength elements and rare earth elements are all mobilized to some extent by the wet component, and the detailed composition of this component is determined. It differs in significant ways from the Mariana component reported by E. Stolper and S. Newman (1994), particularly by having lower abundances of most elements relative to H_2O. The differences can be explained if the slab temperature is higher for the Mariana and the source from which the fluid is derived is more enriched. The ELSC1 damp component is best explained by mixing between the wet component and an E-MORB-like component. We propose that mixing between water-rich fluids and low-degree silicate melts occurs at depth in the subduction zone to generate the chemical diversity of the ELSC1 subduction components. These modified sources then rise independently to the surface and melt, and these melts mix with melts of the background mantle from the ridge melting regime to generate the linear data arrays characteristic of back-arc basalts. The major and trace element framework for ELSC1, combined with different slab temperatures and compositions for difference convergent margins, may be able to be applied to other back-arc basins around the globe.

Citation: Bézos, A., S. Escrig, C. H. Langmuir, P. J. Michael, and P. D. Asimow (2009), Origins of chemical diversity of back-arc basin basalts: A segment-scale study of the Eastern Lau Spreading Center, *J. Geophys. Res.*, *114*, B06212, doi:10.1029/2008JB005924.

1. Introduction

[2] Investigations of magma genesis in back-arc basins have allowed petrologists to address major petrological and geophysical problems such as the effect of water on mantle melting regimes [*Stolper and Newman*, 1994; *Kelley et al.*, 2006; *Langmuir et al.*, 2006], the transport of the subduction component to the back-arc melting regime [*Kelley et al.*, 2006; *Stolper and Newman*, 1994], the geometry of mantle flow in back arc regions [*Pearce and Stern*, 2006], and the range of mantle temperature among back-arc basins [*Kelley et al.*, 2006; *Wiens et al.*, 2006; *Langmuir et al.*, 2006]. The back-arc setting provides unique perspectives on these problems because it is transitional between open ocean ridges, where no subduction inputs are present, and the volcanic front of convergent margins, where subduction inputs dominate. Back arcs provide the well constrained tectonic setting of an ocean ridge, the absence of preexisting crust that often bedevils interpretation of convergent margin magmas, and the fresh glasses quenched at depth that provide pristine magma compositions and the ability to measure volatile contents.

[1]Department of Earth and Planetary Sciences, Harvard University, Cambridge, Massachusetts, USA.
[2]Now at Laboratoire de Planetologie et Geodynamique de Nantes, UMR 6112, CNRS, Université de Nantes, Nantes, France.
[3]Department of Geosciences, University of Tulsa, Tulsa, Oklahoma, USA.
[4]Division of Geological and Planetary Sciences, California Institute of Technology, Pasadena, California, USA.

0148-0227/09/2008JB005924$09.00

[3] Previous studies have shown that back-arc basin basalts (BABB) encompass a distinctive and wide range of chemical compositions from open mid-ocean ridge basalts (MORB) to enriched MORB (E-MORB) to island arc basalts (IAB) and even, occasionally, ocean-island-like samples [*Danyushevsky et al.*, 1993; *Garcia et al.*, 1979; *Gill*, 1976; *Muenow et al.*, 1980; *Pearce*, 1994]. The present consensus on back-arc petrogenesis is built upon several basic concepts. First, the IAB signature in BABB results from the addition to the back-arc source of a component rich in water and large-ion lithophile elements (LILE), derived from the subducting slab, and this component generates an array of sources that melt proportionately to their water content to generate back-arc basalts. Second, this added component contains no high–field strength elements (i.e., Ti, Nb, Ta, Zr, and Hf) [e.g., *Gill*, 1981; *Stolper and Newman*, 1994]. Since high–field strength elements are believed to be immobile in subduction components, they can be used to determine the background mantle composition and the extent of melting for each magma. Third, the mantle wedge to which this component is added may be depleted or enriched MORB-like mantle reflecting the pristine mantle entering the back-arc basin [*Pearce and Stern*, 2006]. Fourth, while all agree that extent of melting increases with water content of the source, some also consider that higher temperatures augment the effect of water on extent of melting [e.g., *Hirschmann et al.*, 1999, *Gaetani and Grove*, 2004; *Kelley et al.*, 2006, and references therein], while others maintain the relationship between water and extent of melting varies little for temperatures appropriate to back-arc basin [*Langmuir et al.*, 2006]. Finally, the detailed composition of the back-arc subduction component was determined by *Stolper and Newman* [1994] for the Mariana back-arc basin, and this composition has been widely used as a general subduction component. Does the subduction component vary from one back-arc setting to another, and if so, what is the cause of the variations?

[4] This paper addresses these various aspects of back-arc basins through a segment-scale study of the northernmost Eastern Lau Spreading Center (segment ELSC1) where there are large compositional variations in zero-age lavas from a restricted length of spreading center where regional-scale variations are minor. This segment occurs within the context of a large regional gradient in the Lau Basin provided by a 400km transect where geochemical and geophysical gradients are pronounced [*Martinez and Taylor*, 2002; *Turner and Hawkesworth*, 1998, *Peate et al.*, 2001; *Kent et al.*, 2002]. The large-scale regional gradients will be addressed in a forthcoming publication. In this paper we present major, trace and volatile element analyses on basaltic glasses from the ELSC1 segment, where fortunately most of the compositional spectrum of back-arc basins is represented, to investigate consensus interpretations of back-arc petrogenesis in a relatively pure natural experiment. What controls variations in BABB compositions for a spatially and temporally highly constrained set of samples?

2. Tectonic Setting

[5] The Lau Basin is an extensional zone located between the Tonga subduction zone, with its overlying Tofua volcanic arc, and the Lau ridge paleo-arc to the west (Figure 1). The ELSC is a first-order 400 km long segment of particular interest because it lies at steadily varying distances from the volcanic front of the Tofua arc. From north to south, the arc-ridge distance decreases from 100 to 40 km, the spreading rate decreases from 97 to 39 mm/a, and the ridge axis shallows from 3000 to 2200 m [*Taylor et al.*, 1996]. The ridge morphology also changes from an axial low on the northern end of the ELSC to an axial high on its southern end, where high water contents in the source may have enhanced magmatic productivity [*Martinez et al.*, 2006]. The ELSC can be subdivided into 3 second-order segments separated by nontransform offsets [*Martinez et al.*, 2006]: the northern ELSC (N-ELSC, 20°32′S-19°20′S), the central ELSC (C-ELSC, 21°26′S-20°32′S), and the Valu Fa Ridge VFR, 22°45′S-21°26′S). We further divide the N-ELSC into two segments, ELSC1 and ELSC2, separated by a small nontransform offset at 20°12.5′S.

[6] This study focuses on ELSC1, the furthest segment to the north. ELSC1 is length 100 km long, lies at 100 ± 3 km from the volcanic front and spreads at a full rate of 88 ± 8 mm/a. Its axial region has the greatest depths and largest rift valley of the entire ELSC [*Martinez et al.*, 2006] and forms a rough floor at 2500–3000 m depth with a small axial valley about 100 m deep and 2 km wide. On the basis of very few samples, previous work [*Hawkins*, 1995; *Kent et al.*, 2002; *Pearce*, 1994; *Peate et al.*, 2001], suggested this segment had the least "back-arc signature" of any segment along the ESLC, owing to the low concentrations of water and other associated elements reported in its basaltic rocks, and consistent with its greatest distance from the volcanic front.

[7] The ESLC1 segment was sampled during Cruise KM04–17 (R/V *Kilo Moana*, 10 September to 15 October 2004). Exact sample locations are given in Table 1 and Figure 1. Sampling was guided by prior survey data from [*Martinez et al.*, 2006], including both ship-based multibeam bathymetry that encompassed the entire ridge axis and surrounding regions and higher-resolution DSL-120 bathymetry and side scan sonar. Together these data provided precise knowledge of the neovolcanic zone and allowed recognition of the areas with the youngest flows. Sampling methods during cruise KM04–17 included dredging, wax coring, and the TowCam device [*Fornari*, 2003] that allowed 8 wax core stations (with accompanying photography) per deployment along transects of about 1 to 1.5 km. Forty-six targets were sampled along this segment with an average spacing of about 3 km and higher density locally near the newly discovered Kilo Moana hydrothermal vent field that occurs in the southern portions of this segment at 20°03′S [*Edmonds et al.*, 2004].

3. Analytical Methods

[8] Major element compositions of glassy pillow rim material were determined using the JEOL JXA-733 electron microprobe at MIT. Analyses were performed in two steps with an accelerating voltage of 15keV. The first run analyzed only sodium using a beam intensity of 5nA (20 μm beam diameter) and counting time of 60 s. The second run, performed on the same analytical spot, analyzed all major elements (including sodium) using a beam intensity of 25nA (10 μm beam diameter) with the following counting times: 60s (SiO_2), 50s (TiO_2), 60s (Al_2O_3), 60s (FeOt), 70s (MnO), 60s (MgO), 60s (CaO), 30s (Na_2O), 70s (K_2O), 100s (P_2O_5).

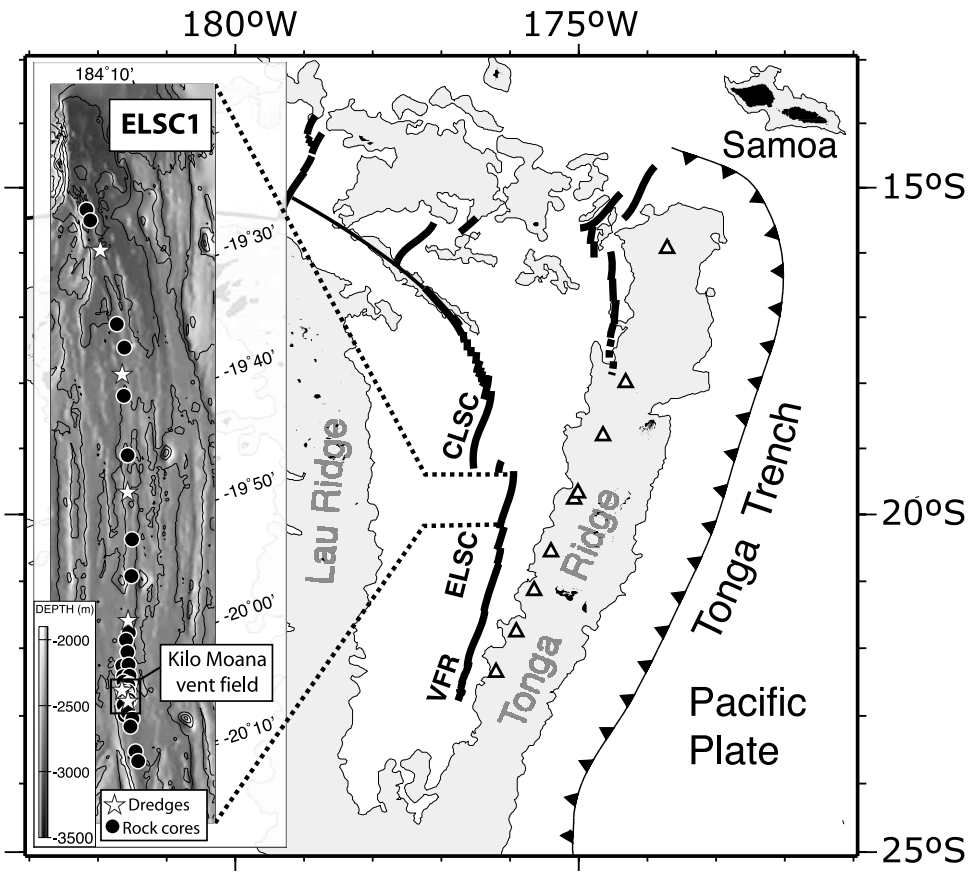

Figure 1. Lau back-arc basin location after *Taylor and Martinez* [2003]. Thick lines indicate spreading centers; white triangles locate arc volcanoes. Encapsulated map: detailed bathymetry of the northernmost second-order segment (ELSC1) of the Eastern Lau Spreading Center. Black dots indicate locations of the rock cores and TowCam samples; stars indicate dredge locations.

Sodium loss caused by high beam intensity was evaluated by comparing the sodium data from 5 and 25nA runs. When the difference in Na_2O measured at 5 and 25nA was greater than analytical error (2% of the total amount) sodium loss was assumed and the 5nA sodium data favored over the 25nA data. Sodium loss is not significant for samples with MgO > 5wt.% and silica <52–53wt.%, which includes all the samples from this segment. The internal glass standard VE32 was analyzed (5 analytical spots) every 25 analytical spots to monitor instrumental drift over time. Individual analyses reported in Table 1 are averages of 5 analytical spots normalized to the VE32 glass standard, for which values are also reported. Major elements reported for DR07–1 were obtained on board during the cruise KM04–17 on bulk glassy rim material using a Direct Current Plasma optical spectrometer instrument. Chlorine, fluorine and sulfur were analyzed simultaneously using the four spectrometers Cameca microprobe at the University of Tulsa. Glasses were analyzed using a 15kV beam and 80nA beam current with a 20 μm beam diameter. Peak positions were counted for 200 s, while background positions on either side of the peak were counted for 100 s each. We verified that the intense beam did not alter the glass during the analyses and lead to the compositional or count rate changes of the elements by checking several glasses (both high and low H_2O content) for count rate variations over consecutive 20 s interval. Reported analyzes are the average of three or four individual spots. Two-sigma precision, based on multiple three-spot analyses of the same basalts glass, are ±0.003% for Cl, ±0.013% for F and ±0.005% for S. Standards were: natural scapolite for Cl, synthetic F-phlogopite for F, and pyrite for S. Instrument drift was monitored using frequent analyzes of a secondary standard: TR154 21D3. The sulfur K-α X-ray peak was scanned in a range of different ELSC glasses using 3 spectrometers simultaneously [*Carroll and Rutherford*, 1988] to verify that the sulfur peak position corresponded to the sulfur peak position of the primary (pyrite) standard and was not measurably shifted toward the S^{6+} position at a lower 2-θ position.

[9] Trace element concentrations were measured on glasses using the X series Thermo ICP-MS quadrupole instrument at Harvard University. For each sample, 50 mg of glass were hand picked under a binocular microscope, discarding all glass chips with visible alteration. Some phenocrysts are inevitably included in the glasses, but phenocryst-rich chips were avoided when possible. The picked glass was ultrasonically cleaned multiple times in milli-Q water baths. Samples were dissolved as glass chips to avoid any contamination during crushing. Dissolutions were performed in a PicoTrace pressure digestion system at a temperature of 200°C and pressure of 30 bars in 1 mL 8N HNO_3 and 0.5 mL ~23N HF for 12 h. The evaporation step was conducted in subboiling conditions using the PicoTrace evaporation system that allows ultraclean evaporation in a closed

Table 1. Samples Locations, Major Elements, Water, Chlorine, Fluorine, and Sulfur Contents of Glassy Pillow Rims From ELSC1[a]

Sample	Longitude	Latitude	Depth (m)	SiO_2	TiO_2	Al_2O_3	FeO_t	MnO	MgO	CaO	Na_2O	K_2O	P_2O_5	SUM	H_2O (Standard Deviation)	Cl	F	S	H_2O Group[b]
RC005	175.961	19.381	3004	50.55	0.97	14.56	9.77	0.19	8.06	12.52	2.27	0.039	0.065	99.00	0.229 (0.007)	0.0120	0.0140	0.1163	low
RC006	175.960	19.396	2970	50.84	1.01	14.71	9.86	0.19	8.00	12.51	2.22	0.041	0.077	99.45	0.225 (0.009)	0.0111	0.0107	0.1133	low
DR05-1	175.958	19.452	2871	50.99	0.92	14.83	9.80	0.19	8.21	12.47	2.23	0.038	0.073	99.75	0.242 (0.009)	0.0123	0.0133	0.1138	low
RC007	175.971	19.550	2697	51.52	0.99	14.58	9.92	0.19	7.77	12.09	2.17	0.052	0.068	99.35	0.330 (0.010)	0.0117	0.0163	0.1090	low
RC008	175.976	19.586	2696	52.35	1.12	14.64	10.65	0.18	7.05	10.99	2.30	0.111	0.103	99.50	0.817 (0.028)	0.0299	0.0070	0.1153	mod.
DR06-1	175.984	19.625	2552	52.17	1.34	14.34	11.55	0.21	6.43	10.33	2.65	0.102	0.106	99.23	0.774 (0.025)	0.0300	0.0165	0.1385	mod.
DR06-T2	175.984	19.625	2552	52.17	1.34	14.29	11.55	0.21	6.43	10.27	2.65	0.105	0.116	99.13	0.921 (0.013)	0.0882	0.0055	0.1220	mod.
DR06-3	175.984	19.625	2552	52.19	1.24	14.34	11.51	0.21	6.52	10.40	2.66	0.101	0.102	99.27	0.811 (0.015)	0.0263	0.0123	0.1338	mod.
RC009	175.993	19.652	2552	51.16	1.21	14.44	10.73	0.18	7.10	11.45	2.47	0.069	0.099	98.91	0.662 (0.009)	0.0577	0.0090	0.1218	mod.
RC010	176.016	19.733	2595	51.50	1.21	14.11	11.34	0.21	7.15	11.11	2.53	0.055	0.092	99.31	0.324 (0.015)	0.0357	0.0167	0.1287	low
DR07-2	176.034	19.795	2730	51.85	1.29	13.93	11.87	0.21	6.88	10.86	2.32	0.047	0.113	99.37	0.365 (0.004)	0.0213			low
DR07-4	176.034	19.795	2730	49.76	0.93	15.56	9.04	0.18	8.06	12.82	2.26	0.040	0.070	98.72	0.719 (0.026)	0.0202	0.0013	0.1113	mod.
DR07-5	176.034	19.795	2730	49.81	0.95	15.46	9.17	0.18	8.04	12.84	2.27	0.043	0.063	98.82	0.754 (0.009)	0.0199	0.0086	0.1114	mod.
DR07-1	176.034	19.795	2730	*49.07*	*0.85*	*16.99*	*9.27*	*0.17*	*8.14*	*12.58*	*2.63*	*0.057*		99.76	0.686 (0.008)	0.0211	0.0118	0.1115	mod.
RC011	176.049	19.850	2627	51.26	1.19	14.33	10.98	0.21	7.30	11.31	2.52	0.058	0.076	99.24	0.440 (0.022)	0.0269	0.0193	0.1223	low
RC012	176.067	19.899	2650	51.27	0.96	14.80	9.70	0.18	8.45	12.47	2.25	0.041	0.065	100.18	0.219 (0.020)	0.0120	0.0097	0.1103	low
RC121	176.106	19.911	2632	51.21	1.22	14.47	10.85	0.19	7.11	11.47	2.38	0.065	0.104	99.07	0.669 (0.021)	0.0175	0.0220	0.1356	mod.
DR08-1	176.094	19.955	2638	51.05	1.07	14.90	10.06	0.19	7.56	11.94	2.21	0.064	0.091	99.13	0.716 (0.003)	0.0215	0.0120	0.1182	mod.
RC123	176.099	19.977	2621	51.02	1.07	14.89	9.87	0.19	7.60	12.12	2.18	0.063	0.095	99.09	0.740 (0.010)	0.0190	0.0143	0.1242	mod.
RC122	176.105	19.985	2551	51.16	1.15	14.85	10.22	0.20	7.15	11.87	2.26	0.072	0.091	99.02	0.994 (0.016)	0.0250	0.0083	0.1238	mod.
RC120	176.108	20.001	2573	51.38	1.21	14.37	10.99	0.21	6.89	11.51	2.39	0.067	0.104	99.12	0.976 (0.008)	0.0182	0.0110	0.1304	mod.
RC119	176.114	20.018	2609	50.65	0.97	15.53	9.21	0.17	7.33	12.29	2.08	0.092	0.085	98.41	1.334	0.0320	0.0087	0.1075	high
RC094	176.121	20.019	2646	51.03	0.85	15.70	8.98	0.18	7.17	12.14	1.99	0.113	0.078	98.23	1.424 (0.105)	0.0424	0.0118	0.0634	high
RC093	176.125	20.033	2645	50.74	0.94	15.57	9.19	0.18	7.29	12.25	2.14	0.105	0.080	98.49					high
RC118	176.122	20.034	2633	50.81	0.90	15.72	8.97	0.17	7.40	12.29	2.08	0.099	0.089	98.53	1.722 (0.043)				high
RC117	176.129	20.041	2639	51.51	1.00	15.48	9.76	0.18	6.62	11.41	2.20	0.119	0.087	98.37	1.796 (0.019)				high
RC022	176.123	20.043	2639	50.61	0.79	15.80	8.46	0.16	7.49	12.50	1.92	0.095	0.055	97.88	1.433 (0.066)	0.0399	0.0040	0.0703	high
CT10-6	176.132	20.052	2630	51.33	1.00	15.47	9.84	0.19	6.58	11.58	2.29	0.125	0.113	98.52					high
RC116	176.131	20.053	2688	50.75	0.89	16.10	8.76	0.17	7.31	12.30	1.92	0.098	0.095	98.39	1.613 (0.035)	0.0504	0.0128	0.0653	high
CT10-1	176.131	20.053	2629	51.67	1.18	14.28	11.18	0.20	7.48	11.52	2.26	0.046	0.089	99.90		0.0105			low
RC090	176.126	20.053	2670	51.14	0.82	15.64	8.67	0.16	7.44	12.44	1.92	0.101	0.085	98.41	1.516 (0.076)	0.0426	0.0050	0.0670	high
RC091	176.132	20.053	2661	51.58	1.18	14.24	11.29	0.22	7.41	11.38	2.23	0.053	0.091	99.67		0.0111	0.0110	0.1290	low
CT10-4	176.133	20.054	2618	51.53	1.06	14.57	10.45	0.19	7.84	11.90	2.15	0.050	0.101	99.84	0.332 (0.003)	0.0092	0.0091	0.1203	low
CT10-8	176.133	20.055	2618	51.22	0.93	15.78	9.41	0.17	6.92	11.93	2.14	0.108	0.098	98.71					high
CT10-3	176.134	20.056	2626	51.91	1.05	14.70	10.50	0.18	7.79	11.90	2.08	0.050	0.096	100.26					low
CT01-1	176.128	20.056	2628	51.16	0.82	15.63	8.62	0.17	7.41	12.35	1.89	0.099	0.086	98.24					high
DR52-1	176.133	20.059	2671	51.25	1.05	14.49	10.65	0.20	7.78	11.86	2.13	0.048	0.087	99.54	0.333 (0.015)	0.0099	0.0203	0.1157	low
RC018	176.133	20.059	2657	51.07	1.01	15.36	9.87	0.18	6.56	11.62	2.23	0.117	0.067	98.08					high
RC092	176.133	20.060	2643	50.94	0.98	15.59	9.43	0.20	6.87	11.96	2.22	0.107	0.072	98.37					high
RC020	176.135	20.063	2652	51.24	1.06	14.35	10.67	0.19	7.83	11.98	2.11	0.039	0.073	99.55	0.239	0.0087			low
RC021	176.131	20.063	2647	51.14	0.83	15.53	8.77	0.17	7.44	12.41	1.96	0.103	0.065	98.42	1.686 (0.021)	0.0446	0.0165	0.0720	high
RC002	176.129	20.065	2644	51.04	0.85	15.50	8.84	0.18	7.41	12.39	1.97	0.103	0.081	98.36					high
DR02-3	176.132	20.070	2661	51.29	0.84	15.50	8.88	0.17	7.40	12.38	1.95	0.101	0.082	98.59					high
DR02-1	176.132	20.070	2661	51.14	0.80	15.83	8.60	0.17	7.32	12.36	1.90	0.100	0.075	98.29	1.461 (0.055)	0.0414	0.0150	0.0704	high
RC019	176.129	20.070	2662	51.07	0.85	15.50	8.83	0.17	7.33	12.24	1.97	0.105	0.068	98.13	1.499 (0.046)	0.0440	0.0105	0.0684	high
RC023	176.137	20.071	2677	51.23	1.04	14.34	10.42	0.18	7.88	11.99	2.12	0.037	0.056	99.30	0.239 (0.013)	0.0098			low
RC016	176.136	20.083	2681	50.94	0.96	15.51	9.43	0.19	6.87	11.82	2.28	0.116	0.076	98.19	1.620 (0.028)	0.0478	0.0073	0.0853	high
RC017	176.141	20.085	2683	51.12	1.06	14.47	10.27	0.21	7.88	12.39	2.24	0.034	0.055	99.73	0.221 (0.007)				low
RC124	176.133	20.096	2684	50.53	0.74	15.73	8.12	0.14	8.47	12.82	1.71	0.088	0.072	98.42	1.574 (0.041)	0.0293	0.0117	0.0797	high
RC015	176.140	20.104	2663	50.49	0.80	15.62	8.63	0.16	8.28	12.66	1.90	0.072	0.059	98.67	1.175 (0.094)	0.0262	0.0130	0.1020	high

Table 1. (continued)

Sample	Longitude	Latitude	Depth (m)	SiO_2	TiO_2	Al_2O_3	FeO_t	MnO	MgO	CaO	Na_2O	K_2O	P_2O_5	SUM	H_2O (Standard Deviation)	Cl	F	S	H_2O Group[b]
RC014	176.144	20.140	2739	51.84	1.11	15.12	10.28	0.20	6.19	10.85	2.20	0.150	0.123	98.06					high
RC013	176.144	20.155	2764	50.89	0.87	15.23	9.09	0.17	7.97	12.71	1.94	0.057	0.068	98.99	0.951 (0.006)	0.0206	0.0103	0.1093	mod.
Measured (N = 427)[c]				50.82	1.72	14.08	11.57	0.19	6.75	10.88	2.97	0.273	0.192	99.44					
Recommended value[c]				50.88	1.86	14.13	11.60	0.21	6.70	10.86	2.97	0.273	0.210	99.69					

[a]Contents are in wt.%.
[b]Low, low water content; mod., moderate water content; and high, high water content.
[c]Internal standard VE32.

beaker system. Samples were then redissolved in 2 mL 8N HNO_3 for 12 h (under the same condition as the first digestion) and reevaporated. The final dissolution is done in 4 mL 4N HNO_3 and the final dilution is 5K (0.050g of sample in 250g of 0.5N HNO_3). ^{72}Ge, ^{103}Rh, ^{115}In, ^{169}Tm, and ^{209}Bi were used for internal standard normalization and the following rocks were used for calibration curves: BHVO-2, W2, DNC-1, and JB-2, as well as the in-house standard Mid-Atlantic Ridge basalt (MAR). The in-house standard K1919, collected from the same lava flow as BHVO-1, was also analyzed and used for drift correction. One sample from the collection (KM04–17 DR50–1) was dissolved and analyzed with each batch of samples to estimate reproducibility between runs. Percent standard deviations for these replicate analyzes over the entire period of geochemical analysis are reported in Table 2 together with standard values, reproducibility and sample analyses.

[10] H_2O was analyzed by Fourier Transform Infrared Spectroscopy at the University of Tulsa using methods and calibration developed at Caltech with slight modifications. Doubly polished glass wafers, 50–200 μm thick, were placed atop a 2 mm thick KBr pellet and analyzed using a NicPlan IR microscope equipped with a HgCdTe detector, attached to a Nicolet 520 FTIR. Optically clear areas of known thickness ($\pm 1\mu$m), 80 $\times$ 80 μm, were analyzed with 256 scans/spot. Absorbance at the broad 3550 cm^{-1} (combined OH^- and H_2O) and 1630 cm^{-1} (molecular H_2O only) peaks was measured after subtraction of interpolated backgrounds. Density was assumed to be 2.8 g/cm^3. Molar absorption coefficients used for all glasses were: 63 l/mol cm for e_{3550} and 25 l/mole cm for e_{1630}. Analyses are the average of 3–4 spot determinations of 3550 cm^{-1} on two separate wafers. Replicate analyses of different wafers from the same specimen were typically reproducible to ±5%. A few samples with $H_2O > 0.7\%$ H_2O contained tiny microlites and did not have optically clear paths so were reproducible to ±7% of the amount present.

4. Results

[11] Major and trace element contents vary substantially within the sample set and define clear systematics that allow separation of the samples into distinct groups.

4.1. Major and Minor Elements

[12] It is particularly noteworthy that the samples have such a large range of water contents, despite the relatively large distance from the volcanic arc and the limited spatial extent. The data encompass almost the same range of H_2O data reported from the Mariana Trough [*Stolper and Newman*, 1994], albeit at much lower K_2O contents (K_2O varies from 0.1 to 0.8 for the Mariana Trough, while it is less than 0.15 for our entire ELSC1 sample suite).

[13] Water contents of the glasses correlate well with other elemental variations. Figure 2 shows that H_2O correlates well with K_2O/TiO_2, and plots along a trend with much lower K_2O/H_2O ratios than basalts from open ocean ridges influenced by hot spot effects (the E-MORB trend shown in Figure 2). The correlation is not perfect, which may result from degassing effects and a small E-MORB component as indicated by the gray arrows in Figure 2. We will show below that there is an E-MORB component within our sample set,

Table 2. ICP-MS Analysis of Trace Element Concentration (p.p.m.) of Glassy Pillow Rims From the ELSC1 Segment[a]

Samples	Li	Sc	V	Cr	Co	Ni	Cu	Zn	Ga	Rb	Sr	Y	Zr	Nb	Sn	Cs	Ba	La	Ce	Pr	Nd	Sm	Eu	Tb	Gd	Dy	Ho	Er	Yb	Lu	Hf	Ta	Tl	Pb	Th	U	Nb/Zr Group
RC005	5.43	41.9	276	339	42.9	81	94	75.2	13.4	0.67	68	26.0	48.7	0.84	0.53	0.008	6.6	1.41	4.91	0.92	5.36	2.07	0.77	3.23	0.59	4.10	0.94	2.65	2.64	0.42	1.40	0.067	0.007	0.33	0.074	0.018	High
DR05-1	5.47	43.4	281	404	44.0	91	94	74.6	11.8	0.64	65	26.1	49.6	0.85	0.58	0.010	5.5	1.38	4.87	0.91	5.39	2.07	0.79	3.27	0.60	4.11	0.93	2.67	2.71	0.43	1.44	0.066	0.008	0.29	0.062	0.019	High
RC007	5.93	43.2	304	236	43.8	77	85	79.6	12.2	0.97	61	26.4	46.5	0.88	0.49	0.014	7.4	1.37	4.71	0.89	5.23	2.00	0.78	3.24	0.60	4.15	0.93	2.70	2.76	0.43	1.38	0.068	0.010	0.34	0.067	0.022	High
RC008	6.74	41.2	347	156	42.1	66	68	87.2	13.2	2.25	69	29.9	53.6	1.15	0.56	0.032	13.9	1.77	5.85	1.07	6.19	2.32	0.85	3.69	0.68	4.70	1.06	3.08	3.14	0.49	1.59	0.087	0.021	0.45	0.098	0.037	High
DR06-1	7.38	41.6	352	31	43.4	38			14.2	2.05	79	34.1	66.3	1.29	0.69	0.026	13.0	2.06	6.89	1.28	7.42	2.73	1.05	4.32	0.78	5.35	1.20	3.45	3.48	0.55	1.95	0.096	0.019	0.51	0.113	0.040	High
DR06-T2	7.39	40.6	354	57	43.0	46			14.3	2.13	79	37.0	75.9	1.57	0.76	0.026	14.3	2.33	7.71	1.42	8.23	2.98	1.09	4.68	0.85	5.77	1.30	3.72	3.77	0.59	2.19	0.112	0.019	0.52	0.132	0.044	High
RC010	6.72	42.5	334	101	45.3	54	92	90.3	14.4	1.14	71	32.3	64.9	1.29	0.67	0.015	9.2	1.90	6.45	1.20	6.92	2.58	0.94	4.08	0.74	5.09	1.14	3.34	3.35	0.52	1.85	0.093	0.011	0.29	0.106	0.032	High
DR07-2	7.38	41.2	362	44	46.9	43	83	100.0	17.2	0.91	66	33.8	66.0	0.98	0.67	0.013	7.8	1.83	6.35	1.19	6.94	2.60	0.96	4.18	0.77	5.30	1.20	3.50	3.58	0.56	1.90	0.077	0.012	0.47	0.087	0.027	Low
DR07-4	4.98	42.0	263	334	43.1	99	96	67.2	14.9	0.78	100	23.5	46.0	0.73	0.50	0.009	6.4	1.36	4.74	0.90	5.26	1.90	0.77	2.99	0.54	3.73	0.83	2.41	2.43	0.38	1.29	0.058	0.011	0.38	0.067	0.021	Low
DR07-5	4.84	41.5	263	359	42.9	93	97	67.3	14.8	0.76	100	23.6	46.2	0.75	0.49	0.009	6.9	1.37	4.77	0.90	5.24	1.89	0.78	2.99	0.55	3.77	0.84	2.40	2.44	0.38	1.30	0.059	0.008	0.39	0.066	0.021	Low
DR07-1	5.74	42.2	299	235	45.0	81	91	79.4	15.8	0.81	88	27.5	54.4	0.83	0.55	0.011	7.2	1.55	5.39	1.01	5.89	2.17	0.84	3.43	0.63	4.36	0.97	2.82	2.84	0.45	1.55	0.066		0.43	0.074	0.023	Low
RC011	6.44	41.1	330	141	45.1	59	91	88.2	16.4	1.10	72	31.2	60.5	1.06	0.64	0.012	8.6	1.72	5.91	1.11	6.43	2.41	0.91	3.88	0.71	4.91	1.10	3.18	3.23	0.51	1.74	0.081	0.010	0.44	0.091	0.028	High
RC121	6.63	42.6	333	75	44.5	53	80	88.5	16.2	1.04	84	31.3	63.3	0.87	0.62	0.013	8.1	1.73	6.10	1.18	6.75	2.54	0.94	3.96	0.72	4.96	1.12	3.22	3.30	0.51	1.85	0.071	0.014	0.40	0.073	0.026	Low
DR08-1	5.85	42.4	319	157	42.2	66	84	79.0	12.3	0.95	80	27.7	55.9	0.75	0.61	0.020	8.9	1.59	5.60	1.05	6.09	2.24	0.82	3.49	0.64	4.37	0.98	2.84	2.87	0.45	1.59	0.059	0.013	0.44	0.066	0.023	Low
RC123	5.79	42.7	304	181	42.7	73	88	77.2	15.0	1.02	86	26.9	54.4	0.73	0.52	0.014	8.3	1.54	5.33	1.02	5.88	2.19	0.83	3.48	0.63	4.34	0.96	2.77	2.90	0.45	1.56	0.060	0.013	0.37	0.066	0.025	Low
RC122	6.27		322	151	41.9	58	87	82.7	13.8	1.16	93	29.0	59.2	0.79	0.61	0.024	10.8	1.75	6.05	1.12	6.49	2.38	0.88	3.69	0.67	4.56	1.02	2.94	2.98	0.46	1.66	0.064		0.40	0.081	0.029	Low
RC120	6.47		335	83	43.6	50	84	87.5	14.2	0.99	84	31.6	63.4	0.87	0.67	0.017	8.7	1.82	6.36	1.19	6.82	2.53	0.95	4.00	0.72	5.00	1.10	3.20	3.22	0.50	1.80	0.070		0.46	0.081	0.026	Low
RC094	4.97	39.1	278	178	37.6	65	89	67.4	12.5	1.48	116	21.2	43.6	0.56	0.44	0.044	19.3	1.40	4.74	0.87	4.97	1.79	0.70	2.72	0.49	3.36	0.75	2.16	2.19	0.35	1.22	0.047	0.021	0.61	0.075	0.033	Low
RC093	5.29	41.9	289	174	40.1	68	86	71.2	13.5	1.44	119	23.2	46.9	0.53	0.49	0.032	16.2	1.52	5.20	0.95	5.42	1.94	0.74	2.94	0.53	3.65	0.82	2.35	2.40	0.38	1.29	0.047	0.020	0.59	0.078	0.029	Low
RC118	5.01	40.7	275	154	39.4	68	83	68.2	14.4	1.44	116	22.4	46.1	0.58	0.45	0.031	14.7	1.45	4.88	0.91	5.20	1.88	0.73	2.88	0.52	3.59	0.79	2.31	2.37	0.37	1.30	0.050	0.019	0.49	0.067	0.031	Low
RC117	5.69	37.9	293	34	40.7	50	67	75.2	15.2	1.63	120	23.9	50.1	0.65	0.48	0.038	18.7	1.59	5.32	1.00	5.56	2.02	0.78	3.07	0.56	3.81	0.84	2.43	2.54	0.39	1.41	0.055	0.023	0.57	0.074	0.036	Low
RC022	4.93	40.4	271	267	39.5	83	91	67.0	12.6	1.32	114	20.8	40.1	0.53	0.48	0.033	14.4	1.35	4.55	0.83	4.82	1.76	0.68	2.69	0.49	3.32	0.74	2.12	2.17	0.34	1.15	0.046	0.019	0.39	0.070	0.030	Low
RC116	5.22	37.9	268	147	38.8	86	85	67.8	14.3	1.26	132	22.1	44.1	0.62	0.44	0.020	11.8	1.44	4.74	0.92	5.12	1.88	0.72	2.88	0.52	3.56	0.80	2.27	2.36	0.36	1.31	0.051	0.018	0.44	0.065	0.029	Low
CT10-1	6.68		341	100	46.1	58	87	90.5	14.3	0.79	71	30.8	60.9	0.83	0.62	0.015	7.6	1.73	6.05	1.12	6.48	2.41	0.90	3.81	0.69	4.83	1.08	3.12	3.18	0.50	1.71	0.066		0.39	0.075	0.024	Low
RC090	4.82	39.9	263	260	39.2	87	91	65.3	13.8	1.36	113	20.5	40.2	0.54	0.41	0.030	15.0	1.32	4.38	0.83	4.68	1.74	0.68	2.67	0.48	3.32	0.74	2.11	2.13	0.34	1.18	0.047	0.019	0.47	0.063	0.030	Low
RC091	6.77	43.5	340	89	46.2	57	84	91.2	14.2	0.83	69	30.7	61.7	0.85	0.60	0.013	7.5	1.67	5.93	1.11	6.49	2.40	0.90	3.83	0.70	4.84	1.08	3.17	3.21	0.51	1.75	0.068	0.011	0.46	0.073	0.024	Low
DR52-1	6.12	43.7	332	154	45.5	69			13.1	0.72	70	28.3	56.2	0.78	0.57	0.008	6.8	1.58	5.55	1.04	6.05	2.23	0.85	3.52	0.64	4.46	1.00	2.92	2.96	0.47	1.58	0.061	0.011	0.39	0.072	0.023	Low
RC092	5.32		286	121	38.9	58	83	70.5	13.1	1.42	116	23.0	48.2	0.62	0.51	0.034	15.6	1.52	5.24	0.94	5.39	1.91	0.75	2.95	0.54	3.67	0.82	2.37	2.40	0.38	1.33	0.050		0.49	0.069	0.032	Low
RC021	4.97	40.3	274	245	38.8	77	91	65.7	12.2	1.33	116	21.3	42.3	0.56	0.42	0.030	15.2	1.36	4.63	0.86	4.94	1.79	0.69	2.76	0.50	3.36	0.76	2.17	2.20	0.34	1.19	0.047	0.018	0.90	0.073	0.030	Low
DR02-1	5.04	41.1	273	265	38.9	79	89	66.4	11.6	1.31	120	21.1	41.6	0.55	0.43	0.031	14.9	1.38	4.63	0.85	4.95	1.77	0.69	2.72	0.49	3.35	0.74	2.15	2.18	0.35	1.19	0.045	0.019	0.50	0.064	0.029	Low
RC019	5.02	39.9	271	230	38.7	77	93	66.9	12.6	1.37	114	21.0	40.6	0.53	0.46	0.034	14.7	1.37	4.62	0.85	4.87	1.76	0.69	2.71	0.49	3.35	0.75	2.15	2.19	0.34	1.16	0.046	0.018	0.41	0.071	0.031	Low
RC023	6.16	43.2	318	197	45.6	74	90	82.9	15.7	0.68	65	28.0	52.9	0.79	0.55		5.8	1.47	5.16	0.97	5.67	2.16	0.81	3.46	0.63	4.41	0.99	2.87	2.90	0.46	1.53	0.064	0.008	0.33	0.068	0.022	Low
RC016	5.62	40.1	299	92	39.8	60	76	72.8	13.5	1.65	126	23.9	48.7	0.55	0.50	0.033	15.5	1.59	5.40	0.99	5.65	2.02	0.77	3.04	0.55	3.77	0.84	2.43	2.51	0.39	1.35	0.049	0.022	0.56	0.079	0.033	Low
RC017	5.79	45.5	291	299	44.2	82	95	77.7	12.1	0.55	66	28.0	53.7	0.79	0.60	0.008	5.1	1.41	5.08	0.96	5.75	2.22	0.84	3.52	0.64	4.47	0.99	2.90	2.89	0.46	1.55	0.063	0.009	0.39	0.059	0.017	Low
RC124	4.52	39.6	249	403	42.9	136	92	61.7	13.3	1.16	97	18.4	35.0	0.47	0.35	0.030	14.2	1.11	3.73	0.71	4.05	1.49	0.59	2.34	0.43	2.94	0.65	1.87	2.01	0.30	1.02	0.042	0.016	0.51	0.054	0.027	Low
RC015	4.92	40.0	260	344	41.5	115	90	66.7	13.9	1.02	92	21.3	41.5	0.58	0.41	0.024	11.7	1.24	4.23	0.82	4.63	1.75	0.67	0.50	2.72	3.42	0.76	2.19	2.27	0.35	1.22	0.048	0.015	0.38	0.058	0.026	Low
RC013	5.06	41.9	275	323	41.4	92	90	68.4	14.7	0.82	85	22.7	43.8	0.62	0.45	0.010	9.8	1.30	4.56	0.85	4.94	1.83	0.72	2.89	0.53	3.64	0.81	2.33	2.39	0.38	1.27	0.054	0.011	0.40	0.063	0.024	Low
Standards																																					
BHVO-2	4.63	31.2	313	289	44.4	114	138	108	20.4	9.38	391	26.9	180	19.8	1.73	0.104	131	15.16	37.14	5.31	24.26	5.93	1.98	0.95	6.24	5.29	0.99	2.50	2.02	0.29	4.45	1.197	0.025	1.60	1.181	0.410	
%RSD	1.1	0.4	1.4	1.6	0.7	1.1	2.2	1.1	1.5	1.2	0.2	0.6	0.4	0.2	1.7	6.3	0.5	0.4	0.2	0.2	0.2	0.2	1.3	0.5	0.8	0.4	0.4	0.4	0.7	0.7	0.4	0.2	2.4	5.7	1.9	1.1	
W2	9.36	35.2	258	89	43.7	68	108	77	18.1	20.11	195	22.2	94	7.9	1.73	0.892	170	10.45	22.84	2.99	12.93	3.21	1.08	0.62	3.76	3.85	0.79	2.19	2.07	0.32	2.44	0.480	0.113	7.91	2.105	0.492	
%RSD	0.9	0.7	1.5	0.9	0.6	0.9	2.2	0.9	1.9	0.2	0.8	0.9	2.0	1.4	4.7	0.9	0.8	0.9	0.6	0.7	0.8	0.6	1.1	0.8	0.9	0.9	0.9	0.6	0.8	1.0	1.9	1.0	0.3	2.6	0.6	0.8	
DNC-1	5.07	31.0	145	288	56.6	251	96	65	13.8	3.71	143	17.9	38	1.7	1.47	0.208	103	3.66	8.14	1.11	5.04	1.41	0.60	0.39	2.10	2.75	0.63	1.86	1.96	0.31	0.99	0.099	0.026	6.24	0.238	0.056	
%RSD	4.8	1.3	2.3	2.8	0.9	0.6	2.1	2.2	1.1	0.9	1.5	1.2	1.7	1.4	21.9	1.9	0.8	0.7	0.9	0.8	1.0	0.9	1.1	0.9	0.9	0.9	0.8	1.1	1.1	1.3	1.8	2.2	2.5	3.0	4.2	3.2	
JB-2	8.25	53.8	574	26	36.1	14	222	108	18.0	6.40	176	24.4	48	0.6	0.61	0.795	219	2.25	6.57	1.15	6.37	2.21	0.83	0.58	3.24	3.92	0.87	2.49	2.53	0.40	1.47	0.051	0.043	5.23	0.255	0.150	
%RSD	1.3	0.8	0.8	1.9	1.4	0.8	0.7	0.7	3.9	1.2	1.2	0.8	1.4	3.4	2.9	2.2	0.6	1.1	1.0	1.1	1.1	0.9	1.1	0.8	1.5	0.8	0.7	1.0	1.0	0.9	1.1	22.0	1.8	2.6	1.1	1.2	
MAR	5.54	39.7	261	325	54.3	151	70	80	14.0	0.93	89	32.1	77	1.5	0.75	0.026	6	2.14	7.18	1.32	7.57	2.77	1.03	0.76	4.24	5.17	1.13	3.24	3.19	0.50	2.07	0.203	0.018	0.35	0.097	0.067	
%RSD	1.3	0.8	1.7	3.6	0.4	1.1	1.3	0.6	7.3	3.9	2.0	0.6	0.8	2.1	2.6	13.4	6.5	1.4	0.6	0.7	0.8	0.4	1.4	0.8	0.6	0.5	0.4	0.4	0.6	0.5	0.9	1.1	7.5	13.0	3.2	2.3	
K1919	4.83	30.5	310	247	50.9	97	147	108	20.5	9.60	394	27.3	183	20.3	1.67	0.097	133	15.55	38.12	5.44	24.77	6.04	2.02	0.97	6.34	5.36	1.00	2.52	2.04	0.29	4.51	1.320	0.024	1.16	1.210	0.420	

Table 2. (continued)

Samples	Li	Sc	V	Cr	Co	Ni	Cu	Zn	Ga	Rb	Sr	Y	Zr	Nb	Sn	Cs	Ba	La	Ce	Pr	Nd	Sm	Eu	Tb	Gd	Dy	Ho	Er	Yb	Lu	Hf	Ta	Tl	Pb	Th	U	Nb/Zr Group
%RSD	3.0	3.1	3.4	2.9	2.9	3.3	4.1	3.5	3.3	3.2	2.9	3.0	3.1	3.1	13.0	4.0	3.1	3.0	3.1	3.1	3.0	3.0	3.5	3.2	2.5	3.1	2.9	3.0	3.3	3.1	3.2	3.1	3.8	5.2	4.8	3.8	
Replicate (N = 11)																																					
DR50-1	8.65	36.3	396	3.75	37.9	16.3	83.6	104	17.3	3.73	125	34.9	82.1	1.2	0.79	0.165	70.6	2.68	7.79	1.58	8.81	3.05	1.12	0.81	4.55	5.51	1.23	3.54	3.63	0.57	2.24	0.092	0.045	1.09	0.154	0.075	
%RSD	2.4	1.8	1.5	17	1.1	3.1	1.9	1.0	5.0	1.7	1.5	1.1	1.4	3.3	2.1	2.6	0.9	0.9	1.1	1.0	1.0	1.3	0.6	0.8	0.5	0.7	1.4	1.0	1.5	1.7	1.3	9.4	1.5	4.8	2.0	1.9	

[a]Concentrations are in ppm.

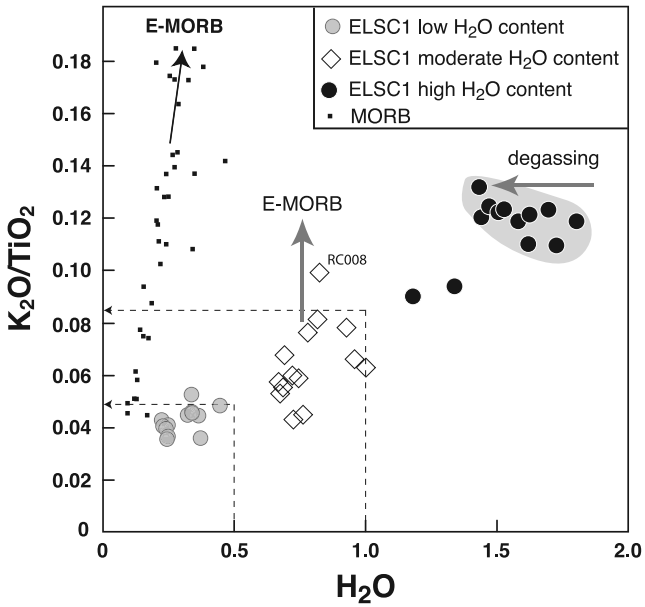

Figure 2. K_2O/TiO_2 versus H_2O contents for open mid-oceanic ridges (small black squares: Fazar sample collection, Azores) and ELSC1 samples (gray dots are low H_2O content; open diamonds are moderate H_2O content; and black dots are high H_2O content samples). Dashed lines indicate how K_2O/TiO_2 has been used as a proxy for water content to classify samples into low, moderate, and high H_2O groups for the purposes of fractionation correction. Solid gray arrows illustrate the effect of water degassing or influence of an E-MORB component. The shaded area refers to samples that are close to the saturation limit of their depth of eruption. These samples may have lost up to 15–25% of their original water by degassing.

which accounts for the excursions to high K_2O/TiO_2 for samples with less than 1% H_2O.

[14] The highest water content samples likely have experienced some degassing. The >1.5 wt.% water contents of several glasses (shaded in Figure 2) are close to the saturation limit for their depth of eruption, and two lines of evidence are consistent with a small amount of degassing. First, their CO_2 contents are very low, although the exact concentrations are difficult to quantify accurately because of interference by the molecular water peak on the carbonate peak in the IR spectrum. Second, their sulfur concentrations are somewhat lower at a given FeOt content compared to MORB [*Mathez*, 1976, P. Michael, unpublished data, 1994] and to ELSC1 glasses with low or moderate water content (i.e., <1 wt.% H_2O). Both these lines of evidence are consistent with the water-rich samples degassing a hydrous volatile phase, and their measured water contents thus represent minimum values. That said, the relatively small depletion in sulfur content compared to many back-arc glasses [*Muenow et al.*, 1991; *Nilsson and Peach*, 1993; *Wallace and Carmichael*, 1992; *Sinton et al.*, 2003], suggests the H_2O loss is small. On the basis of the correlation in Figure 2 and also extrapolations of correlations of H_2O/K_2O with Cl/K_2O, we estimate the H_2O-rich glasses have lost 15–25% of their original water by degassing.

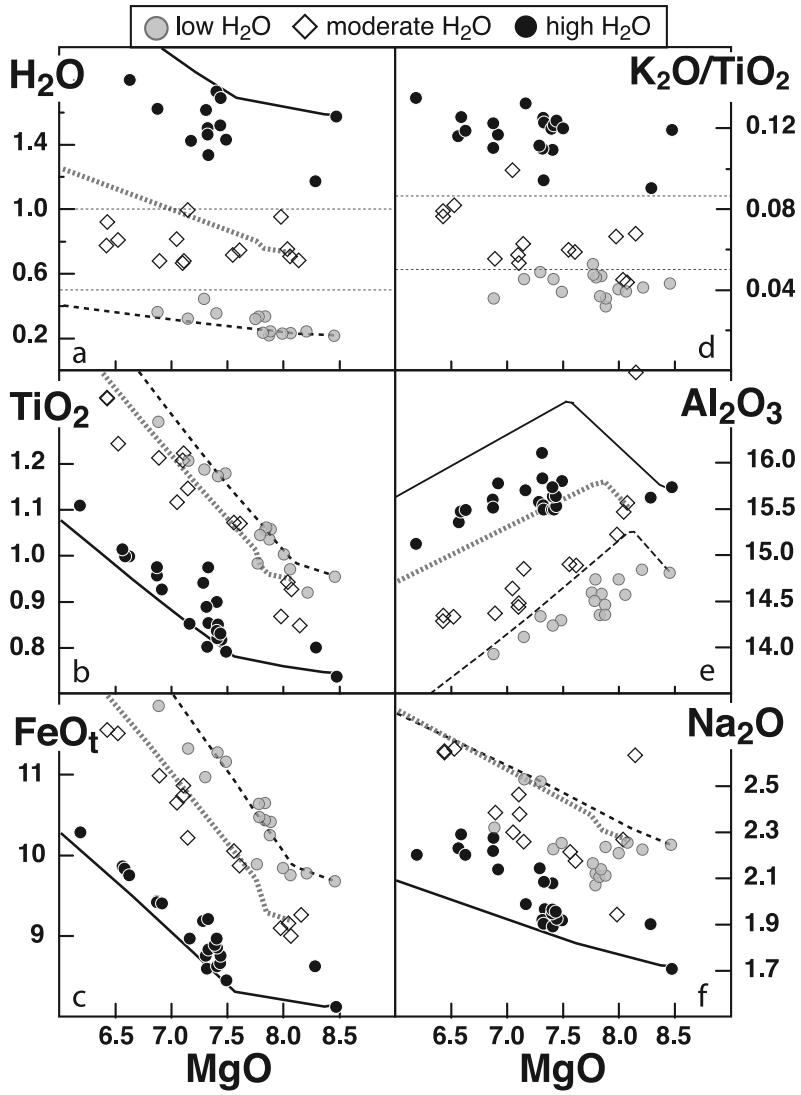

Figure 3. MgO variations diagrams for ELSC1 glasses. The sample grouping is based on the water content (see Figure 2). Liquid lines of descent (LLDs) are computed for each magmatic suite using the hBasalt code (A. Bézos et al., manuscript in preparation, 2009) and the most primitive sample for which water content has been measured. Primitive compositions used for LLDs are thin dashed line, RC012 (low H_2O group); thick dashed line, DR07–4 (moderate H_2O group); and black line, RC124 (high H_2O group).

[15] For the major elements (see Figure 3), glass compositions range in MgO from 6.3 to 8.5% (Table 1), indicating an important influence of crystallization on the chemical variations, the magnitude of which can be appreciated form the liquid lines of descent shown in Figure 3. Obviously crystallization is not the only important factor, since there are significant to large variations in all elements at constant MgO contents. Near ~8%MgO, for example, FeO varies from 8% to 10.5%, TiO_2 from 0.8 to 1.15%, and Al_2O_3 from 14.2 to 15.8%. For minor elements, the differences are even greater, with H_2O and Cl varying by a factor of five at constant MgO, compared to a factor of 8–10 overall, even without making a correction for degassing. To make comparisons more obvious, we divide the samples into three groups on the basis of their water contents, making use of the correlation of Figure 2 to estimate water contents for samples with missing water data. The groups are low ($H_2O < 0.5$ wt.%, $K_2O/TiO_2 < 0.05$), moderate ($0.5 < H_2O < 1$ wt.%, $0.05 < K_2O/TiO_2 < 0.085$), and high ($H_2O > 1$ wt.%, $0.085 < K_2O/TiO_2$). Figure 3 shows that there are coherent variations among major elements that reflect the water contents of the samples. High water samples have higher Al_2O_3 and lower TiO_2, FeO, and Na_2O. These are clearly important variations in parental magma compositions. To address these variations quantitatively requires careful correction to remove the effects of differentiation and retain the residual signal of parental magma variation [*Klein and Langmuir*, 1987].

4.2. Fractionation Correction, Method, and Systematics

[16] Fractionation correction removes the effects of low-pressure crystallization indicated by the liquid lines of descent in Figure 3 to examine differences that are indicative of the parental magmas. In the back-arc setting such correc-

tions are complicated by the fact that water has a significant effect on the Liquid Line of Descent (LLD) due to suppression of plagioclase, and to a lesser extent, clinopyroxene crystallization relative to olivine [*Danyushevsky*, 2001; *Langmuir et al.*, 2006; *Michael and Chase*, 1987; *Sinton and Fryer*, 1987]. The differences are evident for the liquid lines of descent shown in Figure 3, where the kinks caused by the appearance of plagioclase are offset to progressively lower MgO as the water content increases.

[17] As discussed extensively by *Asimow and Langmuir* [2003] and *Langmuir et al.* [2006], correction for low-pressure fractionation leads to different calculated values (particularly for $Ti_{8.0}$ and $Fe_{8.0}$) if the effect of water on LLD is neglected for the most hydrated samples. To account for this effect, we correct the low, medium, and high water groups with different liquid lines of descent according to their water content. The most important parameters that influence the corrections are (1) the MgO value at which plagioclase starts to crystallize and (2) the slopes of the LLDs. Both parameters vary because of variations in water and major elements contents in primitive melts. We have used the updated version of the BASALT code from *Weaver and Langmuir* [1990] (named "hBasalt" (A. Bézos et al., Empirical calibration of olivine, plagioclase and clinopyroxene mineral-melt partition coefficients in presence of water: An improved fractionation model, manuscript in preparation, 2009)) to calculate theoretical wet LLDs for the most primitive samples for each magmatic suite (Figure 3). The pressures of crystallization are estimated following *Michael and Cornell* [1998] to be around 0.2 GPa for all magmatic suites. The computed LLDs agree well with the data for most oxides (i.e., H_2O, TiO_2, FeO, and Na_2O; see Figures 3a, 3c, 3e, and 3f), except for the Al_2O_3 (Figure 3d) where the disagreement results from the fact that very small variations in the MgO where plagiocalse starts to crystallize have a large effect on the precise positioning of the LLD. Petrographic observations in glassy samples from the low–water content magmatic suite reveal indeed the presence of small euhedral crystals of plagioclase in primitive samples (MgO ~8.5 wt. %, RC012) that are likely to be in equilibrium with such primitive melts compositions. In the same way, samples with 8 wt.% MgO from the moderate–water content magmatic suite display euhedral plagioclase. The most primitive sample from the high–water content magmatic suite (RC124, MgO ~8.5 wt.%) has no plagioclase suggesting that this sample is only olivine saturated. We have therefore used these petrographic observations and set the MgO value for plagioclase crystallization at 8.5 wt.% MgO for the low–water content magmatic suite, 8 wt.% MgO for the moderate–water content magmatic suite, and 7.5 wt.% for the high–water content magmatic suite.

[18] Since the theoretical slopes from hBasalt agree well with the observed slopes of each magmatic suite in Figure 3, the hBasalt calculations have been used to determine how the slope varies with starting compositions. The resulting equations are reported in Text S1. Depending on the particular correction scheme needed, the data have been corrected to 8 wt.% MgO or "primitive melt composition" in equilibrium with Fo_{90} olivine (Table S1 and S2, respectively).[1] Provided one relates these compositions quantitatively to calculated mantle melts, the particular normalization point (i.e., 8% MgO or Fo_{90}) is immaterial as long as effects of changes in the plagioclase saturation point are accounted for.

[19] Important uncertainties in the fractionation correction for both hydrous and dry samples relate to the MgO content where plagioclase appears on the liquidus. In addition to the uncertainties associated with the effects of water on plagioclase suppression, small variations in MgO and Al_2O_3 contents can change the point where plagioclase appears by ~0.5% MgO. This is particularly important when working backward to primitive compositions in equilibrium with Fo_{90} olivine. For samples with 8% MgO, if plagioclase appeared on the liquidus at 8%MgO, then the FeO contents of the differentiated liquid are very similar to values in primitive samples. However, if plagioclase appeared at 8.7% MgO, then the FeO content of the 8% MgO sample is 1% higher than the primitive sample. 1% FeO is a large change with important implications for mantle temperature, as discussed further below.

[20] Figure 4 shows the major element systematics of ELSC1 samples after correction for hydrous fractionation. There is a large range of parental magma compositions – $Fe_{8.0}$ varies from 8 to 10.5 wt.%, as $Ti_{8.0}$ increases from 0.7 to ~1 wt.%, $Na_{8.0}$ increases from 1.8 to 2.4 wt.%, and $K_{8.0}$ and $H_{8.0}$ decrease by factors of 3 and 5, respectively (see Figure 5e). The positive correlations among $Na_{8.0}$, $Fe_{8.0}$, and $Ti_{8.0}$ are matched by negative correlations of all these parameters with $H_{8.0}$ (Figures 4c, 4d, and 4e). The ELSC1 data are also significantly offset from what is observed at open ocean ridges (Figures 4a–4b). Even the driest samples from ELSC1 are slightly offset from the open ocean array, and with increasing water content the distance from the normal MORB array increases, with the highest–water content samples having 3 wt.% less $Fe_{8.0}$ than samples with similar $Na_{8.0}$ contents at open ocean ridges.

[21] The striking coherence among major element parameters and water contents are consistent with the global systematics of back-arc basin basalts recently reviewed by *Taylor and Martinez* [2003] and *Langmuir et al.* [2006]. The data array from ELSC1 has less scatter than other data from the literature for various back-arc basins. This likely reflects the good geological control and limited spatial extent of this sample set, since sampling was informed by high-resolution side scan and bathymetry, and the samples are all very young and from a single ridge segment. These data thus provide an exceptionally well controlled and systematic data set for investigating back-arc petrogenetic processes.

4.3. Trace Elements

[22] Figure 5 presents the trace element data from ELSC1 lavas. In contrast to the major elements, the data do not define a single trend but rather split naturally into two groups that converge at the most depleted end to a common point, leading to "V-shaped" data arrays. The two limbs of the "V" can be conveniently divided on the basis of the Nb/Zr ratio. We define low- and high-Nb/Zr groups as those samples with Nb/Zr < 0.017 and >0.017, respectively. The high-Nb/Zr samples have modest water contents ($H_{8.0}$ < 0.7 wt.%) while the low-Nb/Zr samples display a larger range of water content (0.2 < $H_{8.0}$ < 1.7 wt.%) with half of the samples having high water content up to 1.7 wt.% (Figures 5d, 5e, and 5f).

[1] Auxiliary materials are available in the HTML. doi:10.1029/2008JB005924.

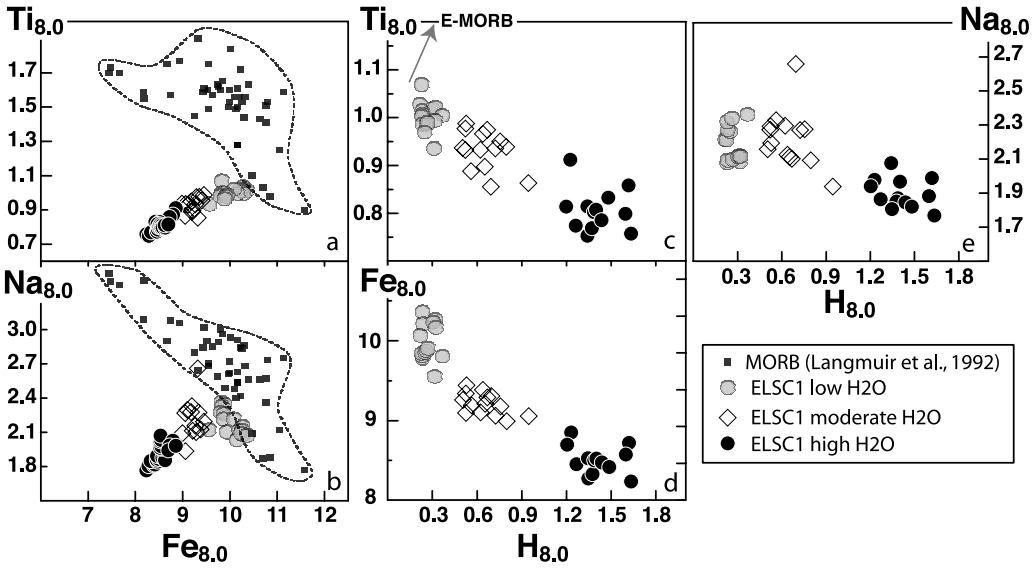

Figure 4. (a)–(b) $Ti_{8.0}$ and $Na_{8.0}$ versus $Fe_{8.0}$; (c)–(d) $Ti_{8.0}$ and $Fe_{8.0}$ versus $H_{8.0}$; and (e) $Na_{8.0}$ versus $H_{8.0}$ for ELSC1 basalts corrected for wet and dry fractional crystallization back to MgO = 8 wt.%. The decreasing $Fe_{8.0}$, $Na_{8.0}$, and $Ti_{8.0}$ content with increasing water content ($H_{8.0}$) is diagnostic of worldwide back-arc basin data and defines orthogonal vectors to the dry MORB arrays in Figures 4a and 4b.

[23] The two distinct trends reflect two distinct styles of enrichment. Samples from the high-Nb/Zr group have high–field strength elements such as Nb and Ta increasing along with incompatible elements such as Ba and Rb, accompanied by only modest increases in water content. Such enrichment is akin to what is seen in E-MORB in ridges around the world. It is not identical, however. Figure 5 also shows the MORB array from open ocean ridges, extending from N-MORB to E-MORB. The high-Nb/Zr group of ELSC1 lavas has higher Ba/Nb, Rb/Nb, and $H_{8.0}/K_{8.0}$ ratios than the MORB array.

[24] The low-Nb/Zr group has the opposite relationship between LILE such as Ba, Rb, K, and Cl and Rb relative to Nb and Ta. As the LILE contents increase, Nb concentrations decrease. The low-Nb/Zr group also has very high water contents and high ratios of LILE to Nb, Zr, and other high–field strength elements. For a given LILE content, low-Nb/Zr samples display higher water contents relative to high-Nb/Zr samples (Figures 5e–5f). This low-Nb/Zr group has strong affinities to an ''arc component'' and differs more strikingly from the MORB array than the high-Nb/Zr group.

[25] Trace element patterns normalized to N-MORB are presented in Figure 6 for the low- and high-Nb/Zr groups. The common features between both groups are (1) all samples are light rare earth element (REE) depleted even relative to normally depleted MORB (N-MORB), with even stronger HFSE depletion (30–80% lower Nb and Ta than N-MORB); (2) all have a positive Pb anomaly; (3) all have increasing highly incompatible element enrichment from U to Cs relative to Nb; and (4) all have very flat patterns from middle to heavy REE, indicating no garnet influence for these samples. There are also contrasts between the high- and low-Nb/Zr groups. The high-Nb/Zr group has a relatively smooth ''U-shaped'' pattern from Cs to Ce. The low-Nb/Zr group has systematic changes with increasing proportions of the wet component. Patterns become progressively more ''W-shaped'' owing to enrichments in U relative to Th and particularly Nb. There are also progressively increasing enrichments in LILE relative to the REE for the low-Nb/Zr samples with higher water contents, and the development of a prominent positive Sr anomaly.

[26] These trace element variations are qualitatively consistent with what is found in other back arcs around the world. *Danyushevsky et al.* [1993] first pointed out the broad diversity of K_2O/H_2O ratios in back-arc basins. More recently, *Pearce et al.* [2005], *Pearce and Stern* [2006], and *Langmuir et al.* [2006] noted the prevalence of both enriched MORB and subduction components in back-arc basins.

[27] From these new and the preexisting data it is clear that back arcs in general are not two component mixtures between MORB mantle and a unique subduction component [e.g., *Stolper and Newman*, 1994]; both types of enrichment need to be considered in the reevaluation of back-arc processes from the linear correlations observed in Figure 5. It is clear from the V-shaped trace element systematics that the chemical variations in ELSC1 are not random mixtures of three components. Instead there is a background mantle, at the point of the ''V,'' to which two discrete components are added. The ''background mantle composition'' has low LILE/Zr ratios (Figures 5a, 5b, and 5c), low LILE concentrations (Figures 5d, 5e, and 5f), intermediate Nb/Zr ratio, and plots close to the extreme depleted end-member of the MORB correlation (Nb/Zr ~0.014–0.017). In order to describe the two enriching components without assigning a particular origin to them, we call the component with lower relative water contents the ''damp component'' and that with higher relative water contents the ''wet component.'' Such nomenclature refers to the water enrichment relative to LILE (i.e., Figures 5e–5f) and not to the actual water content of the components themselves, which cannot be determined on an absolute basis [e.g., see *Stolper and Newman*, 1994].

[28] A coherent model of back-arc petrogenesis for this region needs to define the origin of all three components: a highly depleted back-arc mantle, a ''wet component'' with subduction characteristics that creates the arc-like array, and a

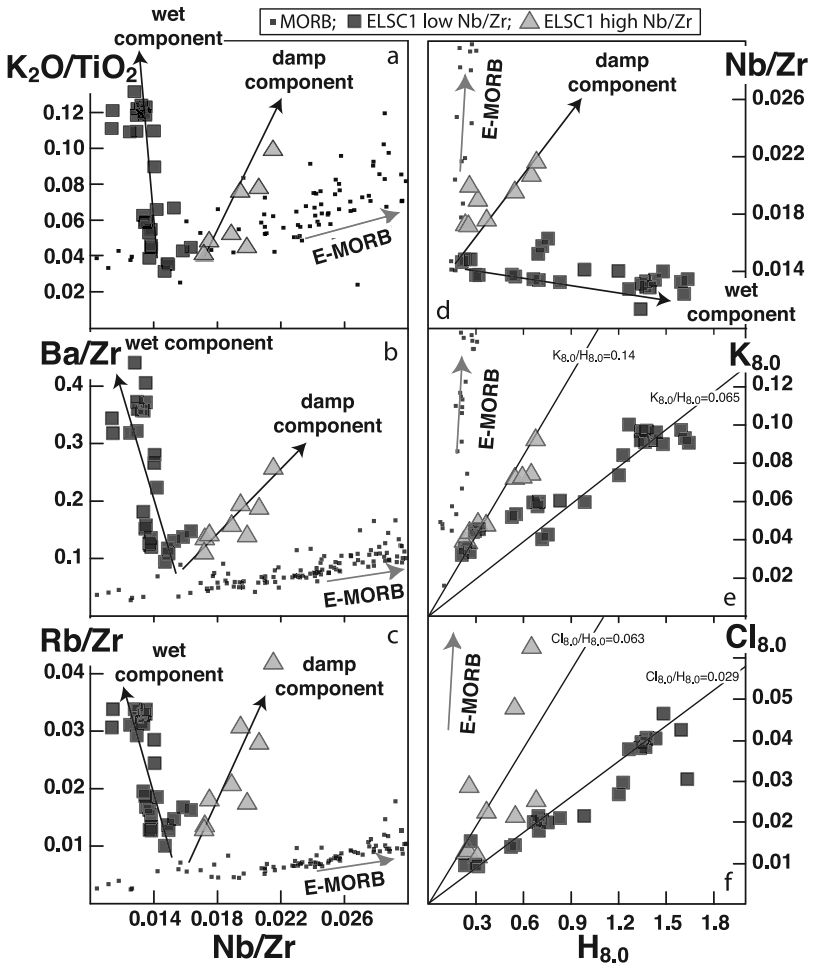

Figure 5. (a)–(c) K_2O/TiO_2, Ba/Zr, and Rb/Zr versus Nb/Zr and (d)–(f) Nb/Zr, $K_{8.0}$ and $Cl_{8.0}$ versus $H_{8.0}$. Data source for Pacific MORB is *Bézos* [2003] and for EPR samples is Petdb (http://www.petdb.org). ELSC1 data define a V shape that suggests mixing between three components: the background mantle that lies at the intersection of both trends, the wet component (low-Nb/Zr trend), and the damp component (high-Nb/Zr trend).

"damp component" that shares affinities with E-MORB and with subduction influences but is discrete from both. It is noteworthy in this data set that the three components are not randomly mixed, but form two discrete arrays that could be interpreted as distinct episodes and locations of binary mixing.

4.4. Spatial Systematics

[29] Both groups of samples come from well-defined geographical provinces along the ELSC1 axis (Figure 7). The low-Nb/Zr wet component group is located exclusively on the southern half of the segment, and the high-Nb/Zr damp component group is restricted to the northern half of the segment (Figure 7a). The transition between the two domains is located at ~19.83°S. There is no obvious change in ridge morphology across this boundary.

[30] Within each of these two regions, variations in major and trace elements described above can occur over very limited spatial scales. This is particularly true in the south where dry (MORB-like) and wet (arc-like) samples were recovered less than 600 m apart from each other. The bimodal distribution of the H_2O/Ce ratio of southern ELSC1 samples (Figure 7b) illustrate well this small-scale heterogeneity with a group of samples having arc-like ratio ~3500 and the other one MORB-like ~400 H_2O/Ce ratio. In the north, the high-Nb/Zr group varies with latitude for Nb/Zr and H_2O/Ce and shows a peak of enrichment (Nb/Zr ~0.021, H_2O/Ce ~1400, RC008) centered at 19° 35.141' (~19.6° S) (Figures 7a and 7b). The close spatial proximity of wet, damp, and dry compositions along a single ridge segment where parameters such as mantle temperature, spreading rate and mantle flow do not vary significantly shows that the source and melting variations coexist at small scale. Because of the systematic chemical variations and the excellent geological control, this region provides an exceptional opportunity for quantitative evaluation of these chemical features, which share characteristics with variations observed in back-arc basins worldwide.

5. Discussion

[31] Problems that can be assessed productively with this data set include the relationship between water and extent of melting in the back-arc setting [*Kelley et al.*, 2006; *Langmuir et al.*, 2006; *Stolper and Newman*, 1994], the origin of trace element variations in back-arc sources [*Danyushevsky et al.*, 1993; *Langmuir et al.*, 2006; *Pearce et al.*, 1995; *Pearce and*

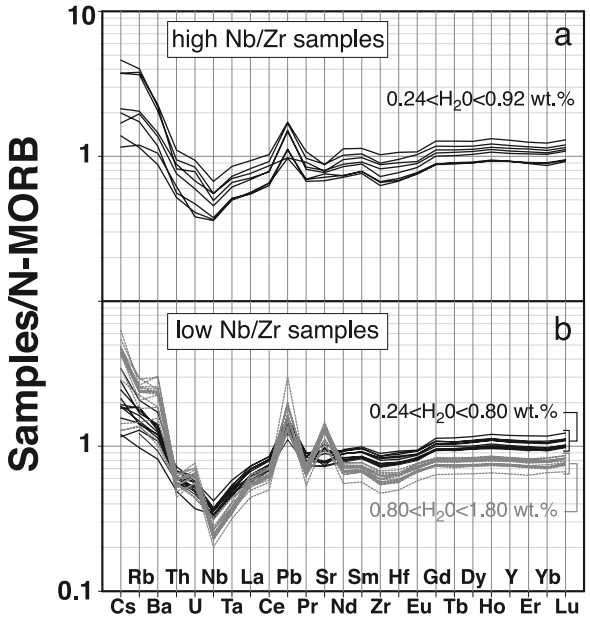

Figure 6. Trace element patterns normalized to N-MORB [*Sun and McDonough*, 1989] for (a) high- and (b) low-Nb/Zr samples. Both groups have very flat patterns from middle to heavy REE, indicating no garnet influence. Subduction mobile elements (i.e., Ba and Pb) are enriched in both groups relative to REE. The low-Nb/Zr group develops a "W" shape with increasing water owing to coupled U enrichment and Nb depletion.

Stern, 2006], and the origin of the distinctive low-Fe major element signature that is characteristic of back-arc basalts [*Langmuir et al.*, 2006, 1992; *Sinton and Fryer*, 1987; *Taylor and Martinez*, 2003].

5.1. Mantle Source Variations

[32] The existence of the V-shaped trends in Figure 5 demonstrates that no single process or component of source variation accounts for the ELSC1 data, and that multiple source variations are required. The question then arises whether either of the trends separately can be produced by different extents of melting of a common source. This question is most simply addressed using Figure 4c where all the data form a single coherent trend of negative slope on the $Ti_{8.0}$-$H_{8.0}$ diagram. All melting curves would have a positive slope on this diagram, and therefore different extents of melting of a common source does not account for the data as a whole. The trend of negative slope illustrated by ELSC1 data is similar to data from back-arc basins worldwide [*Kelley et al.*, 2006; *Langmuir et al.*, 2006; *Stolper and Newman*, 1994; *Taylor and Martinez*, 2003]. This systematic has led to the general back-arc model of source variations in water content leading to greater extents of melting, causing changes in TiO_2 content in the melt [*Stolper and Newman*, 1994].

[33] What are the differences in extent of melting, and what is the overall composition of the added component? The approach to these questions in previous studies has been based on the assumption that the high–field strength elements (Nb, Ta, Zr, Hf, and Ti) are not contributed by the subduction component, and therefore can be used independently to assess the extent of melting by which the basalts are derived. That is, source variations exist for water and other fluid mobile elements, but these are added to a background mantle of constant HFSE composition (which may vary from one back arc to another). From this assumption, for example, TiO_2 contents of erupted lavas can be combined with assumed TiO_2 contents in the source to estimate the extent of melting, from which contents of other elements in the source can be calculated. This approach leads to the diagrams of water content in the source versus extent of melting (C^0_{H2O} versus F) that have been widely presented and interpreted in back-arc settings [*Hirschmann et al.*, 1999; *Kelley et al.*, 2006; *Langmuir et al.*, 2006; *Stolper and Newman*, 1994].

[34] Our new data permit a more thorough evaluation of the assumption of immobility of high–field strength elements, as well as other elements such as the heavy REE (HREE), which should be little affected by the addition of water-rich fluids. The relative mobility of different elements can be evaluated without any starting assumption by making use of the inversion of trace element data, as pioneered by *Minster and Allègre* [1977]. Samples related by different extents of melting form linear arrays on reciprocal concentration plots (RCP) [*Bender et al.*, 1984; *Hofmann and Feigenson*, 1983; *Minster and Allègre*, 1977]. For example, if the HFSE were all to be constant in the source, they would form such linear arrays, which could be inverted for partition coefficients, extents of melting and source concentrations, even if the concentration of other elements such as H_2O changed in the source.

[35] Figure 8a presents RCP for Ta, Ti, and Nb concentrations in primitive melts, i.e., fractionation-corrected melt compositions in equilibrium with olivine Fo_{90}. The low-Nb/Zr data form good linear correlations showing that they

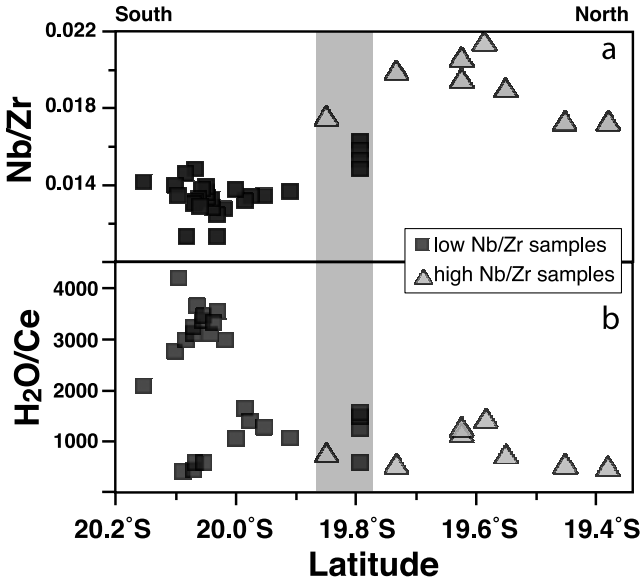

Figure 7. (a) Latitudinal variation of the Nb/Zr ratio showing the "wet" (low-Nb/Zr samples) and "damp" (high-Nb/Zr samples) magmatic provinces. (b) Variation of the H_2O/Ce ratio showing a bimodal distribution in the southern half of the segment, with arc like ~3500 and MORB-like ~400 ratios occurring at the same latitude. The gray band locates the geochemical boundary between the two provinces.

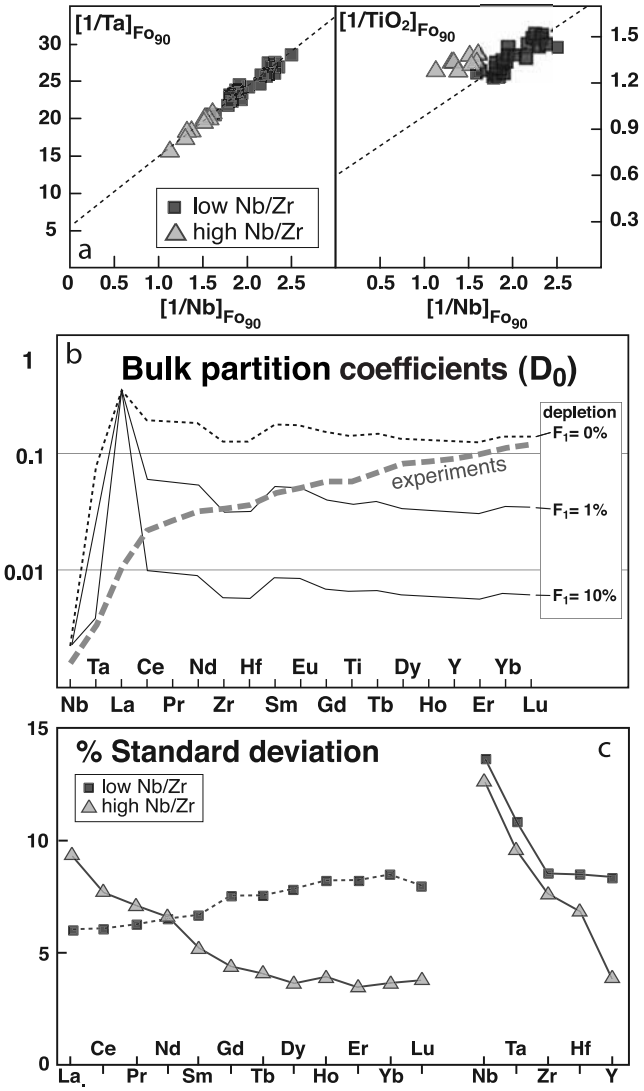

Figure 8. (a) Reciprocal concentration plots (RCP) for low- and high-Nb/Zr samples. The subscript Fo_{90} refers to the primitive concentration of the melt in equilibrium with olivine Fo_{90}. Note that the low-Nb/Zr group defines linear correlation on both RCP while the high-Nb/Zr group does not. The low-Nb/Zr group variability could be therefore interpreted in term of different extent of melting of a single source composition. (b) Trace elements inversion results following *Minster and Allègre* [1977]. Solid lines are computed bulk partition coefficients from low-Nb/Zr samples; dashed gray line is bulk partition coefficients calculated for a peridotite (57:28:15 proportion of ol:opx:cpx) using the experimental Kd compilation from *Donnelly et al.* [2004] and this work. The required Ds from the inversions of the low-Nb/Zr data are inconsistent with any mantle mineral assemblage. (c) REE, HFSE, and Y trace element percent variability for ELSC1 samples corrected for differentiation (Fo_{90} data). The low-Nb/Zr group displays decreasing percent variability with increasing element incompatibility, which is inconsistent with different extents of melting of a common source.

can be reproduced mathematically by the nonmodal melting equation. However, the high-Nb/Zr group does not show such clear systematics in the diagram of 1/Ti versus 1/Nb. This result is not surprising since the high-Nb/Zr samples display E-MORB-like systematics where HFSE behave similarly to other incompatible elements and where source variations are well known. These first-order results suggest that mathematically, the hypothesis of different extents of melting of a common source for the HFSE needs to be explored further for the low-Nb/Zr group and can be ruled out for the high-Nb/Zr group. We therefore consider in the following discussion only the low-Nb/Zr data. We also limit our discussion to relatively "immobile" elements, the HFSE and REE, since the negative correlation between TiO_2 and H_2O and other "fluid-mobile" elements (e.g., see discussion above and Figure 4c) rules out the melting hypothesis for mobile elements.

[36] On RCP the slope S (equation (1)) and the intercept I (equation (2)) recovered from linear regressions in Figure 8a (dashed lines) are functions of the source composition and partitioning behavior as expressed as:

$$S = \frac{C_0^h}{C_0^i} * \frac{1 - P^i}{1 - P^h} \tag{1}$$

$$I = \frac{D_0^i - D_0^h * \frac{1 - P^i}{1 - P^h}}{C_0^i} \tag{2}$$

C^h refers to the concentration of the most incompatible element h in the primitive melt; C^i refers to concentration of a less incompatible element i; C_0^h and C_0^i to the concentration of both elements in the source; P^h and P^i to the distribution coefficient of the actual portion of the solid that is being converted into liquid for both elements; and D_0^h and D_0^i to the bulk distribution coefficient for the element h and i at the initiation of melting. For mantle melting in the spinel stability field, available experiments have indicated that D < P [*Baker et al.*, 1995; *Blundy et al.*, 1998]. Knowing melting reaction for the mantle, partition coefficients and modal abundances, P and D can be related approximately together with, P = 3*D. The constant term comes from the fact that the D is largely controlled by clinopyroxene, which enters the melt preferentially to other mantle phases, and this formulation holds as long as clinopyroxene remains in the residue.

[37] The starting assumptions needed to solve the problem are the values of the concentration in the source and the partition coefficient for the most incompatible element. Variations of D near zero have little effect on the results. Variations of source concentration have strong effects on the source concentration of other elements but have little effect on the relative values of Ds for different elements, which is the most important result. These issues are discussed at length by *Bender et al.* [1984] and *Hofmann and Feigenson* [1983].

[38] We use Nb as the designated reference element, with values of $D_0^h = 0.002$ and $C_0^h = 0.1485$ ppm [*Workman and Hart*, 2005]. We then change the source concentration for Nb by progressively depleting the source to determine the effects of source changes on the relative values of the partition coefficients. Results for the relative partitioning behavior of HFSE, Y and REE are presented in Figure 8b. For all values

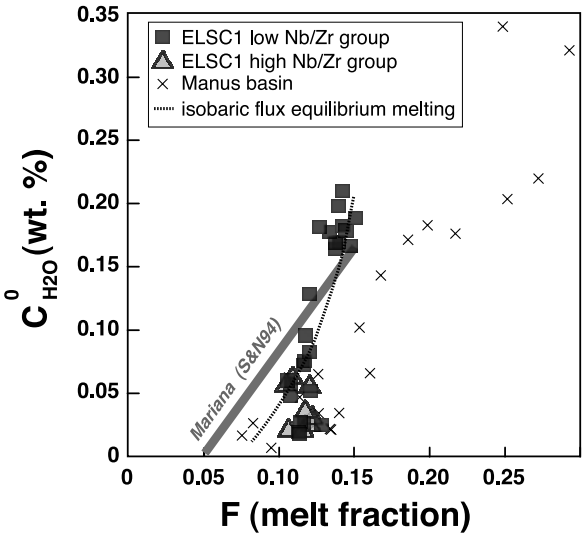

Figure 9. Water content in the source ($C^0_{H_2O}$) versus extent of partial melting (F). Squares are ELSC1 low-Nb/Zr group; triangles are ELSC1 high-Nb/Zr group; crosses are Manus Basin (see *Langmuir et al.* [2006] for data compilation); thick gray line is trend from the Mariana Trough [*Stolper and Newman*, 1994]; and dotted curve is isobaric-isothermal equilibrium flux melting model (P = 1.9 GPa and Tp = 1430°C; see Table 4). The extents of partial melting are estimated from the Lu content in the melt for ELSC1 samples and Y content for Manus Basin samples; the water content in the source is derived from the extent of partial melting and the water content in the primitive melt. The isobaric-isothermal equilibrium flux melting model does not fit the linear relation observed for the low-Nb/Zr group but accounts well for the wet end-member. See discussion in text, section 5.2.

of source concentration for Nb, the results show a characteristic shape of relative values of distribution coefficients, with inverted Ds for light REE higher than D's for the HREE, and a general negative slope of partition coefficient values when plotted in standard order of incompatibility. These results are inconsistent with all experimental data on mantle phases, which show positively sloped partition coefficient variation from Nb through Lu on such diagrams. This negative result applies in general and in detail—for example, the inversion shows similar bulk partition coefficients for Zr and Y, a result that does not agree with the relative compatibility for those elements. This behavior among immobile elements cannot be reconciled with the partial melting of any mantle mineral assemblage (olivine-orthopyroxene-clinopyroxene ± garnet), whether of peridotite, eclogite, or pyroxenite, because all of these minerals have patterns of D's with positive slopes on diagrams such as Figure 8b. Therefore it is clear that variation in extent of melting of a single mantle source is not a viable hypothesis for either the REE or HFSE. The required D's are inconsistent with any mantle mineral assemblage.

[39] The essential aspect of the data that leads to the results in Figure 8b is that for the low-Nb/Zr samples the more compatible elements such as Y and heavy REE vary as much as the highly incompatible elements such as Ta, and more than elements such as La. This causes, for example, the standard deviation of concentrations in the low-Nb/Zr group to be higher for HREE and HFSE than for La (Figure 8c). Varying extents of partial melting cause larger variations in incompatible elements than less incompatible elements, which does not correspond with the data from the low-Nb/Zr samples. These results show that REE and HFSE variations are not consistent with different extents of melting of a common source.

[40] The data call for source heterogeneity caused by significant mobility of HFSE and light REE in the wet component—the HFSE light REE are not "conservative." If Ta, for example, is added with the water that causes a greater extent of melting, then the source and extent of melting effects offset, causing little variability in Ta contents. This result is actually supported by the data from the Mariana back-arc basin. Although *Stolper and Newman* [1994] assumed immobility of TiO_2 to calculate extents of melting and the compositions of the hydrous component, their hydrous component has high Zr and Ta contents, which is inconsistent with TiO_2 immobility, but consistent with the results discussed above. The mobility of the HFSE has the important consequence that they cannot be used reliably to invert for extents of melting assuming a constant source.

[41] We propose as an alternative the use of the heaviest REE, Yb or Lu, to calculate extent of melting. Yb and Lu have moderately compatible behavior in silicate phases, which makes them relatively insensitive to addition of enriched components. For example, addition of 1% of the *Stolper and Newman* [1994] hydrous component leads to a doubling of source concentrations for H_2O and Ba, and a 50% increase for Ta, while Lu concentrations would change by only 5%. Heavy REE are also relatively insensitive to prior source depletion. For example, prior melt extraction of a 1% melt leads to a 10% decrease of Lu in the source, versus a 20% depletion for TiO_2 and a 70% depletion of Nb. Using Lu we can calculate extents of melting (F) for each sample of our suite (C^0_{Lu} = 0.056 ppm; D^0_{Lu} = 0.07), which in turns allow us to determine the source composition for all elements, including the HFSE. This approach then permits us to evaluate how increasing water content in the source affects mantle melting and source composition despite the mobility of the HFSE in the back-arc setting.

5.2. Water and Extent of Melting

[42] Using extents of melting calculated as discussed in the previous section, we can reevaluate the question of how water influences the extent of melting in the back-arc setting. Both low- and high-Nb/Zr samples with less than 0.05 wt.% water in the source show extents of partial melting of about 10–12% and cannot be distinguished in Figure 9. The high-Nb/Zr group does not display sufficient range in water content to generate any clear trend in the C^0_{H2O} versus F diagram. The source water content in the low-Nb/Zr group, however, varies from 0.01 to 0.20 wt.% and correlates positively and, apparently, linearly with the extent of partial melting. Therefore, the low-Nb/Zr group is the appropriate one to evaluate the effect of water on mantle melting and to compare to data and results from other back arc basins.

[43] Figure 9 compares ELSC1 with the Mariana Trough results of *Stolper and Newman* [1994] and the Manus Basin (for which C^0_{H2O} and F have been calculated using the Y content in the lavas instead of Lu). There is good linear correlation between the extent of melting and the source

water content for each of the three basins. The question then becomes how to interpret these relationships.

[44] One model is addition of pure water to a constant temperature and pressure environment, where increasing water in the source increases extents of melting [*Hirschmann et al.*, 1999; *Kelley et al.*, 2006; *Stolper and Newman*, 1994]. A curve for such a model, calculated following the method described by *Langmuir et al.* [2006] is shown in Figure 9 (dotted curve). While the curvature does not match the linear trend defined by ELSC1 data, the end points are well approximated. This model fails, however, when considering other elements such as Fe (see dotted line in Figure 14). The model predicts almost no variation in Fe contents with increasing water in the source, while Fe varies considerably.

[45] These new data provide additional evidence for the controversy over how increased water affects melting as temperature increases. *Kelley et al.* [2006], following *Hirschmann et al.* [1999] and *Gaetani and Grove* [2004] suggest $\partial F/\partial C^0_{H2O}$ (the inverse of the slope on plots such as Figure 9) increases with increasing temperature. *Langmuir et al.* [2006] argue that there is no significant change in $\partial F/\partial C^0_{H2O}$ with change in mantle temperature, and that the apparent change is an artifact of calculations carried out in binary eutectic systems and with the MELTS thermodynamic program [*Ghiorso et al.*, 2002]. The ELSC1 data are particularly suitable for addressing this question, because the samples all come from a limited area where mantle temperature cannot vary, providing a well constrained data set.

[46] As shown in Figure 9, the Manus, Mariana and ELSC1 data all have different F intercepts and slopes. The F intercept should increase with increasing mantle temperature, since it reflects melting under dry conditions. So, for a given source composition, if $\partial F/\partial C^0_{H2O}$ were to increase with ambient mantle temperature, then the F intercept should change systematically, and areas with high $\partial F/\partial C^0_{H2O}$ would have a higher intercept than those with low $\partial F/\partial C^0_{H2O}$. The ELSC1 segment has the lowest $\partial F/\partial C^0_{H2O}$ among the three basins reported in Figure 9 (ELSC1: ~20%F/wt.% H_2O; Mariana: 56%F/wt.% H_2O; manus: 66%F/wt.% H_2O), which would suggest that the ELSC1 has lower mantle potential temperature than both Mariana Trough and Manus. This conclusion is not consistent with any other aspect of the data. Manus and ELSC1 are similar in their major element composition, and all studies agree on the point that the mantle temperature is lower in the Mariana Basin than in Manus and Lau [*Klein and Langmuir*, 1987; *Kelley et al.*, 2006; *Langmuir et al.*, 2006; *Taylor and Martinez*, 2003; *Wiens et al.*, 2006]. Therefore from both theoretical grounds [*Langmuir et al.*, 2006] and the back-arc data, there is no indication of systematic change of $\partial F/\partial C^0_{H2O}$ with mantle temperature for conditions of melt generation in back-arc basins.

[47] An alternative hypothesis to account for the straight correlations observed in Figure 4 and Figure 9 is a mixing process between water-rich and water-poor melts, as proposed by *Langmuir et al.* [2006]. Those with higher water contents would be produced by a different melting environment than those with lower water contents. A physical justification for such a view would call upon the distinct differences in the two sides of the melting regime in the back-arc setting: a wet side with a truncated thermal regime on the arc side and a more normal, drier side far from the arc. Mixing of melts from these two distinct "halves" of the melting regime explains well several aspects of the data. As explained below, such a model allows data sets from different back arcs to have different slopes and F intercepts on diagrams such as Figure 9, predicts the linear trends in the data while the isothermal isobaric water addition model predictions are curvilinear, and also yields large variations in Fe between wet and dry melts.

5.3. Determination of Chemical Components

[48] The extents of melting calculated from the HREE can be used to estimate the chemical composition of the source for every sample in our data set. The systematics of these calculations permit a quantitative assessment of the three different components apparent in the ELSC1 data set— the wet component, the damp component, and the background mantle. To test whether the results for the source compositions reported below depend on the fractionation corrections adopted for this paper, we processed the data set several time with varying MgO values for plagioclase saturation (±1wt. % MgO) for all magmatic suites and obtained the same output compositions for those elements showing variation in concentration of at least 15%. This suggests that results of our calculations reflect true compositional features of the ELSC1 subduction components.

[49] Selected binary diagrams of trace elements versus water content in the source (Figure 10) illustrate the linear behavior of the element systematics, consistent with the mixing scenario inferred from the major elements discussed in the previous section. Similarly to the melt compositions in Figure 5, the source data have a "V shape" that can be interpreted as mixing between a local, dry, background mantle at the depleted intersection of the two trends, and the damp and wet components. For more compatible elements, the relative variations are much smaller, and both data sets plot on statistically indistinguishable arrays. This may show that the wet and damp components share some characteristics in their chemical composition, or this may be a consequence of the limited dynamic range for these elements.

5.3.1. Wet Component Composition

[50] To calculate the wet component we use principal components analysis (PCA) both to determine whether a single trajectory in multiple dimensional space accounts for the data, and also to quantify the wet end-member. Because of the limited compositional variation in the least incompatible elements, we restrict the analysis to elements with a relative range of concentration of least 10%. Data were first normalized to the mean value for each element to give each element equal weight. The PCA results show that a single factor accounts for 93% of the variation, and there are correlation coefficients of greater than 0.7 for all elements with the exception of the HREE and Nb. Using the PCA results, for arbitrary water content in the wet component (50 wt.%) we can determine the concentrations of all other elements. The results for the wet component are given in Table 3 and illustrated in Figure 11. The trace element composition of the ELSC1 wet component shows strong enrichment in fluid mobile elements coupled with a strong Nb-Ta depletion relative to K_2O or La. The elevated Ba/Th, Pb/Nd, La/Nb and Sr/Nd ratios are all diagnostic for a fluid component. This component is also slightly light REE depleted, with chondrite-normalized La/Nd ratios less than 0.8. This suggests

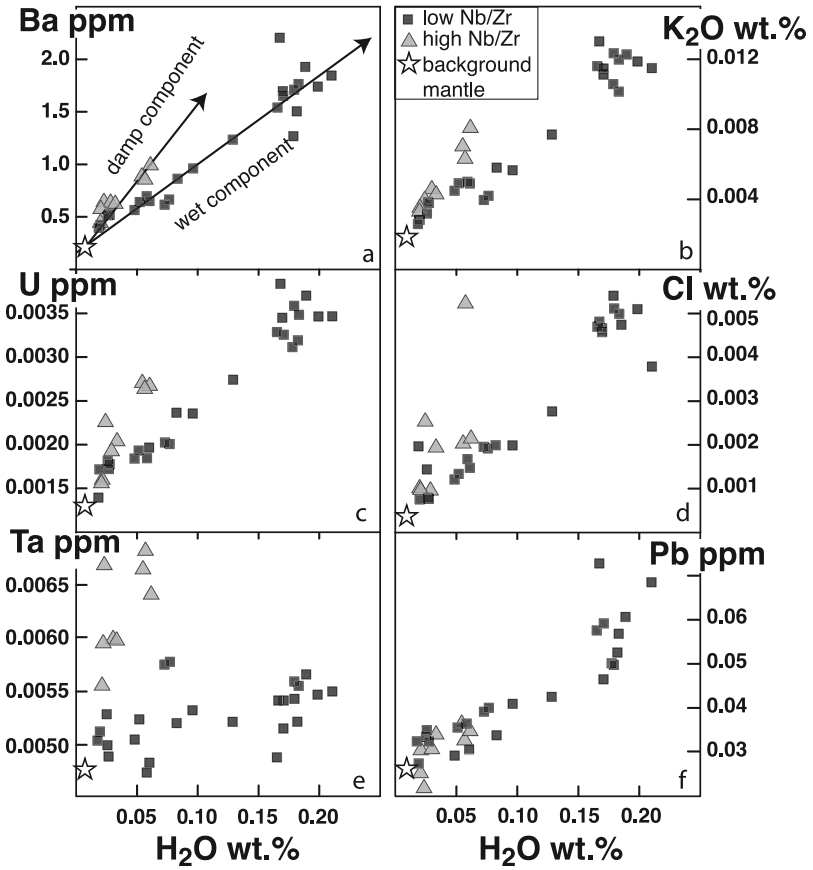

Figure 10. Ba, U, K_2O, Cl, and Pb content versus H_2O content in the source. Black squares are low-Nb/Zr group; gray triangles are high-Nb/Zr group; and white star is calculated background mantle composition (assuming 100 ppm H_2O in the source). Both low- and high-Nb/Zr groups define trends that intersect close to the background mantle composition. The enriched component seen in the low-Nb/Zr group has high relative water content in the source and is called the wet component. The enriched component seen in high-Nb/Zr samples has moderate water content and is called the damp component.

the component is derived from dehydration of depleted ocean crust.

[51] The chlorine-H_2O-K_2O composition of the wet component permits examination of the salinity of the slab-derived fluids. The Cl/H_2O (0.03) and Cl/K_2O (0.46) ratios are greater than typical N-MORB (~0.01 and 0.03, respectively) showing strong chlorine enrichments over H_2O and K_2O in the subduction component. This result is in agreement with previous studies [*Stolper and Newman*, 1994] and corresponds to fluid salinity of about 3.7 wt.% NaCl (following *Kent et al.* [2002]), which is similar to other back-arc basins. However, the Cl/K_2O and Na_2O/H_2O ratios differ among and within back-arc basins [*Kelley and Hauri*, 2007; *Kent et al.*, 2002]. For example, the Cl/K_2O ratio is ~0.46 for the ELSC1 wet component, 0.14 for the Mariana Trough [*Stolper and Newman*, 1994], and can vary from ~0.05 to 0.5 for the East Scotia, Woodlark, Mariana, and North Fiji back-arc basins [*Kelley and Hauri*, 2007].

5.3.2. Damp Component Composition

[52] Principal components analysis was also applied to the high-Nb/Zr group using elements showing variation in concentration of at least 10%. As for the wet component, this filter eliminated all the HREE and Y from consideration. A single factor accounts for 74% of the variation, and correlations between the factor and the elements was greater than 0.5 for all elements considered except for Zr and Hf. The much smaller range of concentrations in the high-Nb/Zr group compared to the low-Nb/Zr group leads to a less well-constrained result (a more variable source component could have the same effect). Because of these limitations, the composition of the damp component is less reliably determined than the wet component. A specific chemical composition for this component is nevertheless proposed in Table 3, using an arbitrarily assigned water content of 30 wt.% and the PCA results.

[53] The damp component displays a geochemical signature that is intermediate between the wet component and an E-MORB-like component. It has no Nb or Ta anomaly and is slightly LREE-enriched (La/Nd ~ 1.1 times chondrites), characteristic of an enriched signature (Figure 11). However, it also has slight positive Pb and Sr anomalies, and a low Th/U ratio, indicating some subduction influence.

5.3.3. Background Mantle Composition

[54] The V-shaped arrays of data suggest a common background mantle composition to which both components are added. We estimate this composition from the principal component analysis of the wet component by fixing arbitrary the water content of the background mantle at 100 ppm. The

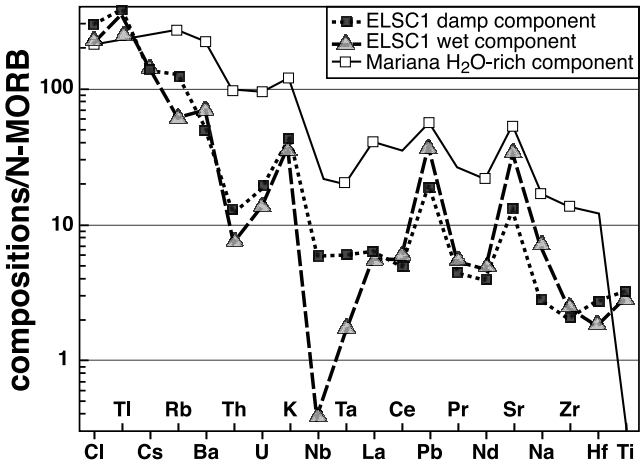

Figure 11. ELSC1 wet (dashed line with gray triangles) and damp (dotted line with black squares) components and Mariana Trough water-rich component (solid line with white squares) [*Stolper and Newman*, 1994] normalized to N-MORB [*Sun and McDonough*, 1989]. Missing elements in the Mariana Trough composition are interpolated by eye. Note the generally lower levels of the ELSC1 components compared to the Mariana Trough and the relatively high Cl, Tl, and Cs of ELSC1. The negative Nb-Ta anomaly observed in the wet component vanishes in the damp component with a slight increasing light REE enrichment relative to heavy REE. Such a signature is diagnostic of a low-F melt contribution in the damp component.

resulting chemical composition is exceptionally depleted in Nb (~0.06 ppm) and LREE (La/Nd ~ 0.4 times chondrites) relative to the estimated depleted mantle [*Salters and Stracke*, 2004] 0.21 ppm Nb and La/Nd ~ 0.6 times chondrites, respectively. It also clearly shows the influence of the subduction setting, with slight enrichments of, for example, Cl, Rb, U, K_2O, Na, and Pb (i.e., Ce/Pb ~ 16). This composition clearly reflects an earlier melting event that led to the depletion in highly incompatible elements such as Nb, and also the addition of a small amount of subduction component to produce less depleted levels of subduction mobile elements.

5.4. Origin of the Components

[55] Partial melting and dehydration processes of the subducted oceanic crust, sediments and hydrated peridotite could generate in theory a large compositional spectrum of metasomatic agents (e.g., silicate melts, carbonatite melts, or hydrous fluids). Understanding the problem of recycling processes at subduction zones requires therefore studying these various components and the mass transfer processes by which they are added to the mantle wedge. Quantitative estimates of metasomatic fluid compositions related to arc volcanism have been provided by numerous studies [*Eiler*, 2001; *Eiler et al.*, 2007; *McCulloch and Gamble*, 1991; *McDade et al.*, 2003; *Stolper and Newman*, 1994]. All fluid compositions share to first order the same characteristic of LILE enrichment over HFSE, which is best explained by the addition of slab and/or sediment derived fluids to the mantle wedge. For example, previous studies on the Lau-Tonga arc-back arc lavas have shown that water-rich fluids from the altered oceanic crust dominate the subduction input to the mantle wedge while the sedimentary input appears to be moderate [*Ewart et al.*, 1998; *Hergt and Woodhead*, 2007; *Turner et al.*, 1997]. In the following section we attempt to place constraints on the contribution of fluids and partial melts from the altered oceanic crust and/or the sediments to the chemical compositions of the ELSC1 components.

5.4.1. Origin of the Wet Component

[56] The sediments subducted at the Tonga trench have been sampled at DSDP sites 595/596 and site 204. The ~70 m thick sediment section lithology is largely dominated by clay and chert materials with a small contribution of metalliferous sediments [*Plank and Langmuir*, 1998]. Locally (site 204), sediments are dominated by volcaniclastics derived from the nearby Louisville seamount chain that have an E-MORB-like signature [*Turner and Hawkesworth*, 1998]. Dehydration and melting experiments on the pelagic clays unit from site 595 [*Johnson and Plank*, 1999] provide experimental data that match the natural conditions in the Lau back-arc basin. Furthermore, the estimated chemical composition of average Pacific Altered Oceanic Crust (AOC) from *Kelley et al.* [2003] coupled with experimental data on trace element partitioning during slab dehydration [*Kessel et al.*, 2005] allow us to approach quantitatively the problem of the subduction component origins.

[57] Figure 12a shows that no single component accounts for the compositions of either the wet or the damp components for the ELSC1. Trace element ratios such as Pb/Ce and Ba/Th are diagnostic for fluid addition in subduction systems, since Pb and Ba are fluid mobile elements compared to Ce and Th, which are mobile in silicate and/or sediment melts

Table 3. Compositions of the ELSC1 Source End-Members

Elements (ppm)	Wet Component	Damp Component	Background Mantle
H_2O[a] (wt.%)	50.00	30.00	0.0100
Cl (wt.%)	1.30	1.73	0.00031
K_2O (wt.%)	2.82	3.11	0.0019
Na_2O (wt.%)	18.1	7.06	0.200
TiO_2 (wt.%)	3.50	3.99	0.110
Tl	0.49	0.53	0.00049
Cs	1.01	0.92	0.00014
Rb	34.1	69.2	0.039
Ba	432	322	0.251
Th	0.87	1.42	0.0048
U	0.62	0.82	0.0014
Nb	0.86	13.2	0.061
Ta	0.18	0.77	0.0049
La	13.8	15.4	0.115
Ce	39.6	35.6	0.424
Pb	11.2	5.76	0.024
Pr	6.80	5.73	0.085
Sr	2983	1131	5.59
Nd	33.0	27.6	0.529
Zr	178	145	4.80
Hf	3.54	5.42	0.156
Sm	9.35	-	0.213
Gd	9.28	-	0.357
Tb	-	-	0.069
Dy	-	-	0.483
Ho	-	-	0.110
Y	-	-	3.16
Er	-	-	0.332
Yb	-	-	0.348
Lu	-	-	0.054

[a]Water content fixed arbitrary to calculate all other elements.

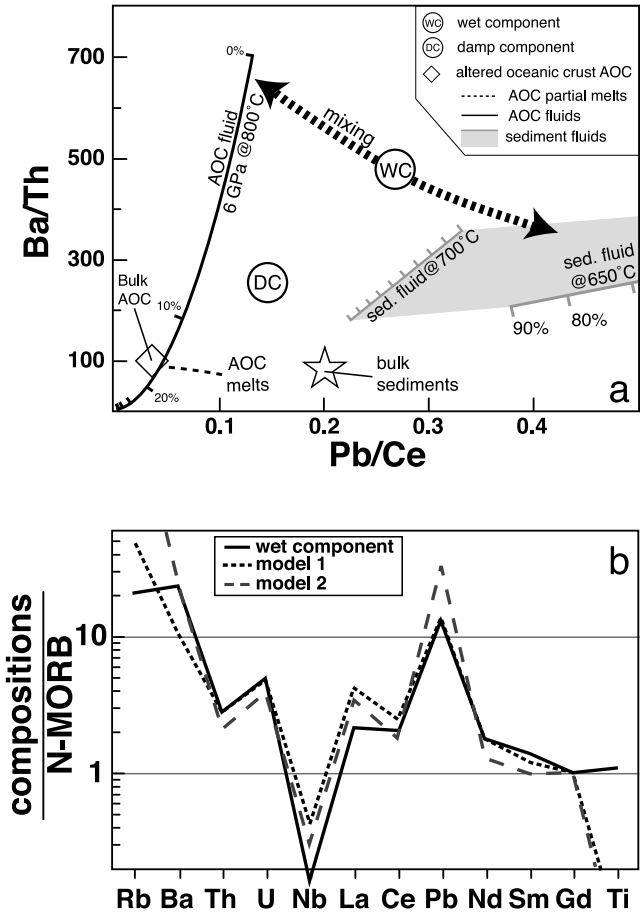

Figure 12. (a) Ba/Th versus Pb/Ce showing the ELSC1 wet and damp components with the bulk chemical composition of altered Oceanic Crust (AOC) and pelagic sediments (red clays from *Johnson and Plank* [1999]). Dashed black line is AOC partial melts ranging from 0.1% to 20%; solid black line is composition of the fluids produced by progressive dehydration of the AOC (ticks marks: % dehydration); and gray lines and shaded area are composition of the fluids produced by progressive dehydration of the bulk sediments (for temperatures ranging from 650° to 700°C). The dashed double arrows illustrate mixing between AOC fluid and sediment fluid to produce the chemical composition of the ELSC1 wet component (see section 5.4.1). (b) Quantitative attempts to reproduce the wet component composition by mixing AOC fluid and sediment fluids in proportion of 80:20 for model 1 (if considering previous AOC dehydration at the volcanic front) and ~50:50 for model 2 (without considering previous dehydration).

[*Elliott et al.*, 1997; *Miller et al.*, 1994]. But neither the bulk chemical compositions of the Pacific AOC, nor sedimentary clays, nor fluids or melts derived from these compositions correspond with the wet and dry ELSC1 components. As illustrated by the thick dashed line in Figure 12a, a mixture between sediment and AOC derived fluids is a possible origin for the subduction components. A physical mechanism is possible movement of an AOC fluids through overlying sediments to incorporate both AOC and sediment signatures.

[58] Figure 12b quantifies mixing processes between AOC and sediment-derived water-rich fluids to fit the ELSC1 wet component composition. Because the active volcanic arc is the first consequence of slab dehydration, it is conceivable that back-arc basin magmatism relates to a second generation of AOC- and/or sediment-derived fluids. In order to evaluate the effect of previous dehydration related to the arc volcanism, our first model (model 1: dotted line in Figure 12b) involves a Rayleigh distillation process to calculate the composition of the fluids released from the AOC and sediments into the back-arc region. This model has three free parameters: the extent of volcanic front predepletion of the AOC, the same for sediments, and the mixing ratio between these two previously depleted sources. If dehydration at the volcanic front removes about 90% (by mass) of water in the sediment and 10% of water in the AOC, then we can reproduce fairly well the wet component composition in all elements but Ti. Such a model requires that 80% of the fluids come from AOC and 20% from sediment. The second calculation (model 2: dashed line in Figure 12b) mixes the water-rich fluids from AOC and sediment without considering any previous dehydration event. Model 2 reproduces the ELSC1 wet component almost as well as model 1 (only the fit for Pb is noticeably worse) but requires a higher contribution from sediment fluids (~47%). The contribution of sediment melts has also been tested (not shown) and ruled out because their REE patterns are too fractionated to match the wet component.

[59] In general the LREE-depleted composition of the wet component argues strongly for its derivation from subducted ocean crust rather than sediment. Neither model calculated reproduced the high Ti concentration of the ELSC1 wet component, although they do reproduce fairly well the negative Nb anomaly. The models we test are nonunique solutions. They show that the wet component is consistent with subduction processes involving water-rich fluids delivered from the dehydration of a depleted oceanic crust, and also that some process is necessary to mobilize small extents of the HFSE and Th along with the classical suite of elements mobile in subduction fluids.

5.4.2. Nature of the Damp Component

[60] Because of the limited dynamic range of the data, the detailed composition of the damp component is less well constrained. There are general observations, however, that are robust. The damp component has high Nb and does not have the negative Nb anomaly characteristic of most subduction components, while having also elevated levels of some subduction mobile elements. These observations are evident, for example, in the Nb/La ratio of ~0.9, a common oceanic mantle value, accompanied by Ba/La of ~20, near the values associated with arc lavas. Another characteristic of the damp component, in contrast to the wet component, is that it is LREE-enriched (see Table 3).

[61] This combination of characteristics can be compared to the wet component on a diagram of Ba/Zr-Ta/Zr (Figure 13), where high Ba/Zr is characteristic of subduction components and high Ta/Zr is characteristic of enriched mantle components and not of subduction components. The damp component trajectory is intermediate between the wet component and an OIB-like component trajectory (E-MORB trend in Figure 13).

[62] It has recently been suggested that the fluid released during serpentinite dehydration might impart a unique geochemical signature on island arc lavas. Sepentinite mantle

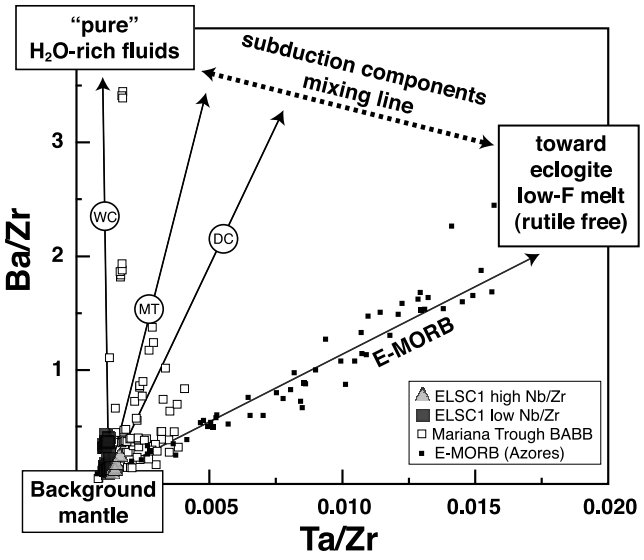

Figure 13. Ba/Zr versus Ta/Zr for ELSC1 (big black squares and gray triangles), Mariana Trough (white squares: compilation from *Langmuir et al.* [2006]), and E-MORB samples from the Mid-Atlantic Ridge (small black dotes: Azores, FAZAR sample collection). WC is ELSC1 wet component (Table 3); DC is ELSC1 damp component (Table 3); and MT is Mariana Trough H_2O-rich component [*Stolper and Newman*, 1994]. The thick double-arrowed dashed line illustrates the mixing processes between subduction components (H_2O-rich fluids and low-F eclogite melt) generating the required chemical variability of the ''composite subduction components'' (e.g., WC and DC). Lines with a single solid arrow illustrate mixing between the back-arc background mantle and the composite subduction components. This model based on ELSC1 samples provides a general framework to interpret the chemical diversity of Mariana Trough and other back-arc basin samples, but detailed ratios and abundance ratios may also be influenced by slab composition and temperature (see discussion in text, section 5.5).

contains ~12 wt.% H_2O, has extremely LILE-depleted signature relative to eclogite, and has the ability to carry water to greater depths (~150–250 km) than can either altered MORB or sediments [*Schmidt and Poli*, 1998]. Such fluids, however, cannot account for the chemistry of the damp component, because they would have very high H_2O/trace element ratios and very high Pb/Ce ratio. For example, *Tenthorey and Hermann* [2004] report Pb/Ce ratio up to 2.2 for serpentinite and dehydration of serpentinites would further increase the Pb/Ce ratio in the released fluids phase to reach values as high as ~21 [*Tenthorey and Hermann*, 2004]. This is inconsistent with the low Pb/Ce of the damp component of ~0.16.

[63] Another potential subduction component could be derived by low extents of melting of peridotite or AOC. Such melt would mobilize both fluid mobile and fluid immobile elements, which is the main requirement for the generation of the damp component. In order to evaluate this hypothesis, we mix the water-rich subduction component with low-degree melts from peridotite or rutile-free eclogite (as illustrated by the dotted line Figure 13). In order to produce the V-shaped systematics, this mixing event needs to take place first to form the damp component that mixed further with the ambient mantle. This conceptual two-step mixing would produce the V-shaped trends and linear arrays that are prominent characteristic of the ELSC1 data.

[64] We can envision two processes by which such mixing may come about. One would be the progressive melting of the mantle wedge by the wet component as it passes through the wedge. As the water-rich material migrates through the wedge, it samples a larger and larger source volume of mantle material, leading effectively to a very low degree melt of peridotite. E-MORB and ocean island basalts have the trace element characteristics of very low degree melts added to their source regions [*Donnelly et al.*, 2004; *Workman et al.*, 2004], and hydrous melt migration might be a mechanism to mimic such a process. Alternatively, low-degree melts of subducted eclogite, at depths where TiO_2 solubility has increased enough to render rutile unstable, might add enriched low-degree melts to the mantle wedge where they could mix with a hydrous component to produce the damp component. In both scenarios, the wet and damp components would be the result of different mixing proportions of water-rich fluid and low-degree melts components.

5.5. Damp and Wet Components in the Context of Other Back-Arc Basins

[65] The exceptional geological control and sample density of ELSC1 lead to the clear delineation of two distinct components contributing to back-arc basin geochemical variations. The question naturally arises whether such systematics are also seen in other back-arc basins.

[66] *Pearce et al.* [2005] have already noted that geochemical variations in the Mariana Trough require both subduction and an OIB-like enriched components. They ascribe the OIB-like variations to variations in the composition of the mantle wedge entering the back arc region. Alternatively, the Mariana Trough, like ELSC1, could reflect the mixture of two distinct components produced by subduction zone processes themselves. Figure 13 shows the Mariana Trough data, and that in general they lie between the wet component and the E-MORB trajectories. In general, compared to ELSC1 data, the Mariana Trough samples have extremely variable proportions of E-MORB-like component. Following this line of reasoning, the subduction component calculated by *Stolper and Newman* [1994] may not be the true wet subduction component, but instead a mixture of the two components we have identified.

[67] This does not explain the most striking difference between the Mariana component and the ELSC1 components, which is the difference in overall abundance levels, particularly of the REE and Zr. As apparent in Figure 11, the Mariana component is a factor of 5–10 enriched (relative to the same water content) for most elements.

[68] This difference may result from a difference in the thermal environment of the slab, and the less depleted overall source signature of the Mariana relative to the Lau Basin. *Kessel et al.* [2005] showed that fluids at higher temperatures have far greater concentrations of most incompatible elements, and particularly the REE and HFSE, than fluids at lower temperatures. The ELSC1 wet component comes from a highly depleted source, and the very rapid convergence rate of the northern Lau Basin could lead to a relatively cold slab temperature. In contrast, the Mariana component clearly

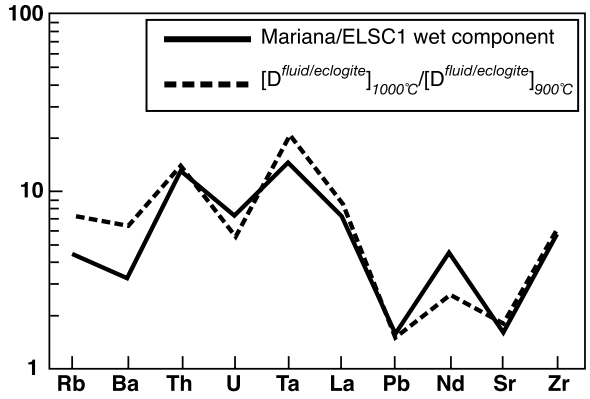

Figure 14. Possible explanation for the differences between ELSC1 wet component and Mariana Trough component. The solid black line is the ratio of the Mariana component to the ELSC1 component. Dashed line is the ratio of fluid enrichments determined by *Kessel et al.* [2005] for 1000° and 900°C, acting on a depleted MORB for ELSC1 and an E-MORB for Mariana [from *Sun and McDonough*, 1989]. A higher-temperature slab and more enriched crust could explain the differences between the two subduction components.

reflects a more enriched source, and the slower convergence rate could lead to a warmer slab. The combination of these two factors accounts well for the difference in compositions between the Mariana and ELSC1 wet components, as shown in Figure 14. The *Kessel et al.* [2005] partition coefficients also can account for the fact that the ''hydrous component'' has high Th contents, even though Th is viewed as immobile in hydrous fluids. Compared to the ELSC1 subuction components, the very high Th content in the Mariana component would reflect therefore both the higher slab temperatures and the more enriched source. As noted earlier, there are certain ratios (such as Cl/K_2O) that are not consistent with this simple framework, and we note also the relative discrepancies for Ba and Rb, and therefore greater complexity is required in detail.

5.6. Mantle Temperature Beneath the ELSC1

[69] Mantle temperature beneath the Lau Basin can be inferred from the extents of melting calculated from the trace element data as discussed above, and the major element contents of the wet and dry end-members. The dry end-member of back-arc major element arrays has been commonly used to calculate mantle temperature for back-arc basins [e.g., *Kelley et al.*, 2006; *Klein and Langmuir*, 1987; *Langmuir et al.*, 2006, 1992; *Taylor and Martinez*, 2003; *Wiens et al.*, 2006]. This dry end-member requires either correction for fractionation all the way back to primitive compositions in equilibrium with the mantle or alternatively forward fractionation of calculated primitive compositions to a reference value of MgO such as 8 wt.%. Both of these methods are equivalent, and depend on either forward or backward fractionation corrections.

[70] There are complexities for back arcs as compared to open ocean ridges that must be taken into account for an evaluation of mantle temperature from major elements. The Na_2O content in the source can vary either by depletion owing to previous melt extraction, or enrichment owing to high Na_2O contents of subduction components (i.e., see Table 3), or both. Therefore the assumption of near constant Na_2O values is particularly problematic in the back-arc setting. As we mentioned earlier, TiO_2 data may suffer from the same problems.

[71] FeO is a major element in the mantle with a partition coefficient near unity and is far less sensitive to prior melt extraction or subduction fluid addition compared to incompatible elements such as Na_2O and TiO_2. FeO data are therefore favored to model mantle temperature beneath back-arc basins. There is still uncertainty in how to relate FeO contents of primitive magmas with those of erupted lavas owing to the fractionation offset between mantle melts and observed compositions. As mentioned earlier (section 4.2), FeO contents are very sensitive to the onset of plagioclase crystallization. For ELSC1, FeO increases by 1.7 wt.% for every 1 wt.% decrease in MgO once plagioclase appears on the liquidus. Following *Langmuir et al.* [1992], 1.7 wt.% variation on the FeO contents of primitive melts translates into ~100°C variation in mantle potential temperature. Because FeO contents are particularly important for evaluation of mantle temperature, uncertainty in the onset of plagioclase crystallization leads to uncertainties in calculated temperature.

[72] For ELSC1, we constrain plagioclase onset using petrographic observations, where plagioclase first appears at 8.5% MgO for the low–water content magmatic suite (Figure 3), in agreement with most dry magmatic suites from open ocean ridges. In this case, the FeO contents of the primitive melts at Fo_{90} are 9.7 wt.% FeO (Figure 15). This constraint along with the extent of melting calculated above for the dry end-member of about 10% can be fit by pooled fractional melting of mantle with potential temperature of 1450°C and Na_2O and TiO_2 contents of 0.25 wt.% and 0.11 wt.%, respectively, that are slightly depleted relative to open oceanic ridge source 0.27–0.3 wt.% for Na_2O and 0.13–0.145 wt.% for TiO_2.

[73] The FeO contents of the wet end-member at Fo_{90} are considerably lower ~8.8 wt.% FeO (Figure 15), while calculated extents of melting are higher (14%). Melting models are also constrained by our knowledge of the H_2O contents of the source. A good fit to the wet end-member results from equilibrium melting of a mantle source enriched in H_2O, Na_2O, TiO_2, and K_2O at 1.8–2.0 GPa with slightly lower mantle potential temperature ~1430°C. This depth corresponds approximately to the initiation of the largest increments of melting in the dry melting regime discussed above. Source compositions, mantle temperature and calculated melt compositions for the wet and dry end-members are reported in Table 4 and shown in Figure 15.

[74] The need for equilibrium melting at moderate pressures, with no inherited garnet influence from depth, suggests that the hydrous portions of the mantle rise without melt segregation until they reach shallow levels. At these levels, the equilibrium, hydrous melt is delivered to the melting regime where it can mix with the fractional melts being produced by ''normal'' ridge processing. Then the array of observed compositions reflects mixing between the moderate-pressure equilibrium melts and the polybaric fractional melts (Figure 15).

[75] In the open ocean environment, the high mantle temperatures required by the ELSC1 data would produce

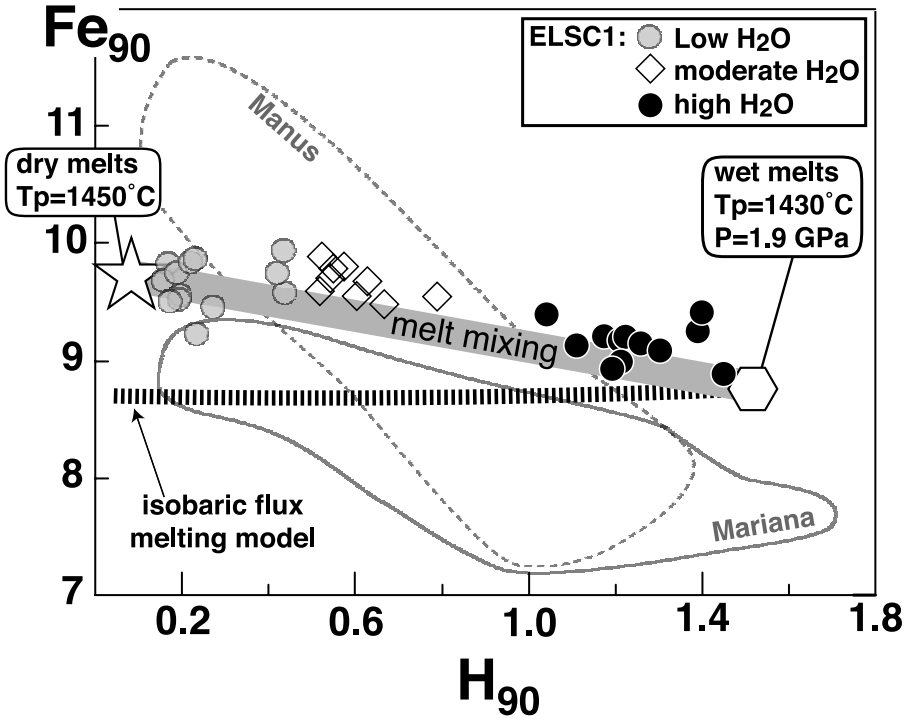

Figure 15. FeO versus H_2O contents of primitive melts (i.e., Fe_{90} versus H_{90}) for ELSC1 samples. The Mariana Trough and Manus Basin fields [*Langmuir et al.*, 2006] are shown for comparison. Thick gray line is mixing between dry fractional polybaric melts (mantle potential temperature: Tp = 1450°C; see Table 4) and wet equilibrium isobaric melts (Tp = 1430°C and P = 1.9 GPa; see Table 4). Thick dashed line is isobaric flux melting model with water content in the source varying from 0.01 to 0.2 wt.% (Tp = 1430°C and P = 1.9 GPa). This latter model fails to generate the large variation in FeO observed for ELSC1 and other back-arc basins basalts [*Langmuir et al.*, 2006]. The ELSC1 major and trace elements systematics are best explained by shallow mixing between dry and wet melts.

crustal thickness of 10km, inconsistent with the inferred 6–7 km of crust for this region [*Martinez et al.*, 2006] and the ridge depths of about 2700m. We speculate that a solution to this paradox may be the asymmetry of the melting regime in the back-arc environment, where the "dry side" delivers its full complement of melt to the ridge axis, while the "wet side," impeded by lower temperatures and the complex flow and melt segregation regime associated with subduction, corner flow, and arc volcanism delivers a smaller volume of melt.

[76] It is also important to note that the temperatures and extents of melting we are able to calculate for this region require heterogeneity in the TiO_2 and Na_2O contents of the mantle sources. Low Na_2O and TiO_2 values for the dry end-member are due to the depletion of the mantle wedge, as reflected in the very low Nb contents of ELSC1 magmas. The higher Na_2O and TiO_2 contents of the wet source reflect additions of Na_2O and TiO_2 in the wet component.

[77] Our calculated mantle temperature ~1450°C (Table 4) is similar to previous estimates [*Kelley et al.*, 2006; *Langmuir et al.*, 2006; *Wiens et al.*, 2006] calculated using similar methods with FeO contents. The northern Lau Basin is considerably hotter than the Mariana Trough (or East Scotia basin, ~1350°C) and slightly cooler than the Manus Basin [*Kelley et al.*, 2006; *Langmuir et al.*, 2006; *Wiens et al.*, 2006]. It is noteworthy that all 3 data sets, ELSC1, Mariana Trough, and Manus, trend toward wet end-members with lower FeO contents in Figure 15. This feature reflects the need for of low-pressure reequilibration for wet melts as seen in worldwide back arc basin data. This latter result contrasts

Table 4. Melting Models Parameters and Results for Values Corrected to Fo_{90}

	Dry Melt	Calculated Dry Melt	Source Composition	Wet Melt	Calculated Wet Melt	Source Composition
FeO wt.%	9.8	9.7	8.3	8.8	8.8	8.3
MgO wt.%	15	14.5	38.1	13.5	13.6	38.1
H_2O wt.%	0.10	0.09	0.01	1.50	1.52	0.22
Na_2O wt.%	1.75	1.76	0.25	1.55	-	0.30
TiO_2 wt.%	0.80	0.76	0.11	0.64	0.64	0.13
K_2O wt.%	0.020	0.020	0.002	0.090	0.090	0.013
F (%)	10	10	Pooled	14	14	equilibrium
T (°C)			1450			1430
P (GPa)			fractional			1.9 GPa

markedly with the systematics of melting for open ocean ridges.

6. Implications for the Physical and Chemical Model

[78] Understanding recycling processes at subduction zones requires integration of petrological and geochemical constraints with the physical environment. The ELSC1 data set provides several new constraints related to the mass transfer processes by which subduction components are added to the mantle wedge. We now consider different schematic models that include constraints from the ELSC1 data in the context of a ''subduction factory.''

[79] The mixing relationships between dry melts (background mantle), wet melts, and damp melts argue against a model where a single hydrous component is added to a background mantle that varies in composition from N-MORB to E-MORB. Such a model would create ''V-shaped trends'' that converge at the wet component, and diverge toward background mantle composition. This is not consistent with the ELSC1 data, which converge at the depleted background component and require diverse enriched components. The slab-derived subduction components mix at depth in the mantle to generate both damp and wet components, and then migrate to shallower levels beneath the ridge where they will finally mingle and mix with dry melts prior to eruption.

[80] Because a fully satisfactory model should account for both major and trace elements, we need also to take into account the equilibrium melt generation that is necessary to explain the low FeO content and the lack of a garnet signature in wet lavas. This latter constraint implies a lack of interaction between wet melts, or subduction components, and the mantle wedge over a distance of ~100 km. We can invoke several physical processes to chemically isolate melt or fluid flows from the mantle matrix and delay mixing of dry and wet melts to shallow levels. *Davies and Stevenson* [1992], *Hall and Kincaid* [2001], and more recently, *Langmuir et al.* [2006] proposed a diapirism model as a possible mechanism. It is also possible to envision a model where the fluid delivery to the ELSC1 melting regime occurs via high-porosity dissolution channels such as those invoked by *Spiegelman and Kelemen* [2003] to preserve chemical heterogeneities all the way to the surface at mid-oceanic ridge. An interaction between the two mechanisms is also likely. *Hall and Kincaid* [2001] showed with laboratory experiments that the formation of diapirs leads to the formation of a network of fossil conduits within the mantle wedge. Such conduits are for subduction components direct and fast pathways through the mantle wedge to the back-arc region.

[81] The cartoon in Figure 16 shows qualitatively how these geochemical and petrological constraints might be reconciled with a physical model. As the slab is heated, water is released from the slab, followed by subsequent low extents of partial melting either within the slab or in the overlying mantle wedge (stage 1 in Figure 16). Variable mixing ratios between the hydrous fluid and the low-F melts account for the chemical diversity of the subduction components (e.g., wet and damp components). Once these subduction components are formed, they leave the source and migrate toward the shallower part of the mantle wedge. They may focus rapidly to form either buoyant unstable parcels of mantle (stage 2 in Figure 16) or high-porosity channels. It is likely that melting occurs at depths in the mantle where garnet is a stable phase. However, if melt and residue ascend together, any garnet signature in the melt will be erased if garnet in the source is melted out or if the residual garnet is later converted into clinopyroxene and spinel, with clinopyroxene subsequently melted out. This would explain the lack of a garnet signature in back-arc data. In Stage 3 (Figure 16), the diapir crosses the base of the ELSC1 melting regime at ~3 GPa (i.e., 100 km depth) and rises through the ELSC1 melting regime where, owing to melting processes, local mantle porosity increases and favors the extraction of wet melts from the rising diapir. The mixing between wet and dry melts (Stage 5 in Figure 16) generates the linear correlations observed in Figures 4 and 5. As shown in Figure 7, the geographical distribution of the damp and wet components (high- and low-Nb/Zr samples, respectively) along axis may suggest that two different diapirs reached the ELSC1 segment. From this geographical distribution of heterogeneities we can constrain the size of the parcels of buoyant mantle to be of the order at least 10 km. All wet samples in the southern section of the ELSC1 segments are found within a ridge section 10 km long, as are the high-Nb/Zr samples (Nb/Zr > 18) in the northern ELSC1 section.

[82] The constraints from the major elements imply mixing of melts formed by two different physical processes −polybaric fractional melting for the least hydrous melts, and isobaric equilibrium melting for the hydrous end-member. Conceptually this could happen by delivering equilibrium melts to the bottom of the melting regime and having these melts participate in the further melting that takes place at shallower levels. This implies processes intermediate between mixing of melts and mixing sources.

[83] This raises the question of our calculation of component compositions in Table 3, which is based on variations in source content followed by different extents of melting, rather than mixing of melt from distinct sources. Since all the melts form linear arrays, however, this makes little difference in the calculated result, which we confirm by calculating the composition of the wet component using only the background mantle and the most hydrous melts. Because of the problems associated with a two-point regression, we prefer values based on the entire data set.

[84] We cannot be definitive on the physical model that would account best for all ELSC1 geochemical and petrological constraints. Critical constraints are the lack of garnet signature and the low-Fe contents that require equilibration of wet melt at low pressure. In addition, it is also conceivable that the chemical variations of subduction components are related to the melt and/or fluid flow through the mantle wedge, with for example high-porosity channel flow favoring the assimilation of peridotite low-F melt in water-rich fluids en route to the surface. Developing numerical models to test these ideas could provide new insight into the structure of subduction components inputs beneath back-arc basins.

7. Conclusion

[85] The major and trace element systematics from the ELSC1 segment bring new and strong constraints on hydrous mantle melting in this back-arc basin, on the origin of the

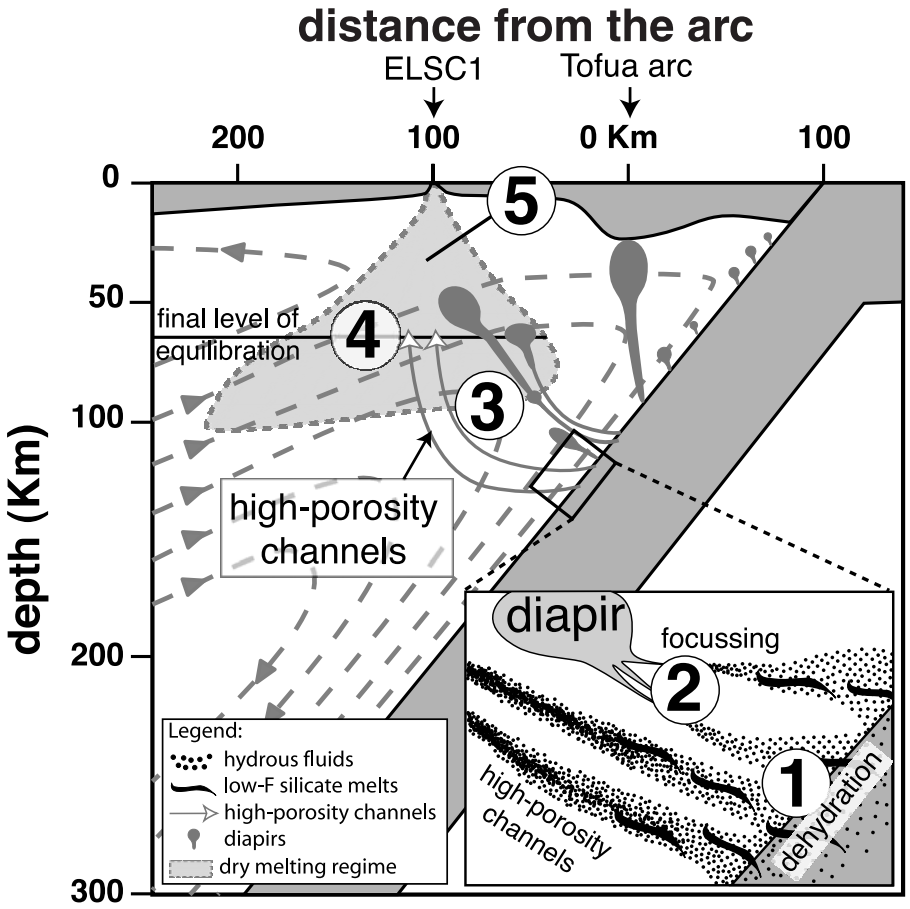

Figure 16. Cartoon showing the proposed physical model that could account for the ELSC1 data systematics. Stage 1 is slab dehydration processes and generation of low-degree silicate melts; stage 2 is fluid focusing and accumulation in the ambient mantle and formation of parcels of buoyant material and/or transit of the subduction components through high-porosity channels. The mixing ratio between low-degree melt and hydrous fluid fixes the composition of the subduction component (wet versus damp). Stage 3 is when the diapir ascends toward the shallower part of the mantle wedge as a closed system; stage 4 is the final level of equilibration ~65 km below the seafloor for wet component melts; the diapir system now opens, or the subduction components are released by high-porosity channels in the ELSC1 dry melting regime therefore generating low-pressure equilibrium mantle melts; stage 5 is when during the final ascent, dry melts and welt melts coexist and mix together to form the ELSC1 chemical systematics.

subduction components and on the physical processes by which they are added to the mantle wedge.

[86] We show that the background mantle composition is influenced in the southern half of the ELSC1 segment by a water-rich subduction component (wet component) while in the northern half the contaminant by a less water-rich component (damp component) showing geochemical affinities with both E-MORB and arc-type enrichments. The enrichment of water is characterized relative to LILE enrichment. The inversion of fluid immobile elements (HFSE, REE, and Y) requires mobility of HFSE in the wet component and shows that the least affected elements are the heavy REE. The damp component shows unambiguously strong enrichments in the HFSE (e.g., Nb-Ta) as indicated by its E-MORB geochemical affinity.

[87] We use Lu to estimate the extent of melting, recalculate the water content in the source, and propose a reevaluation of the effect of water on melting in back-arcs basins. ELSC1 data show clearly that in the value of $\partial F/\partial C^0_{H2O}$ cannot be understood as a simple function of mantle temperature as suggested by *Kelley et al.* [2006], *Hirschmann et al.* [1999], and *Gaetani and Grove* [2004]. More importantly, we further demonstrate that the flux melting model, i.e., isobaric isothermal addition of water to the mantle wedge, does not reproduce the ELSC1 major element systematics, especially the large FeO variations that are negatively correlated to water content. The successful model we propose mixes dry polybaric melts with low-pressure equilibrium wet melts.

[88] Principal component analysis permits calculation of the composition of the wet component, the damp component and the background mantle compositions. The wet component originates mainly from dehydration of the subducting altered oceanic crust, with some contribution from a subducted sediment source. The damp component can be accounted for by mixing processes between a low-F melt and a water-rich (wet) component. This latter model may provide a general framework for understanding the geochem-

ical variations observed in worldwide back-arc basin basalts, but does not fully account for differences between the ELSC1 and Mariana subduction components. We note that fluids formed from more enriched ocean crust at higher temperatures are consistent with the difference between Mariana and ELSC1 component compositions. Finally the mixing relationships between the background mantle and the wet and damp components require a physical model that delays mixing of the subduction component–driven melts with the upwelling-driven melts from the back-arc melting regime until relatively low pressure. The diapir and/or high-porosity channel flow models might both satisfy the requirement of chemical isolation of wet melts from the surrounding solid matrix and low- to moderate-pressure equilibrium of wet melts.

[89] Because most back-arc basin spreading centers are subparallel to trenches, a strong physical and compositional asymmetry appears between the two ''halves'' of the melting regime [*Langmuir et al.*, 2006]. The arc side is supplied by water-rich subduction components (perhaps as diapirs) while the far side is fed with dry pristine mantle. Back-arc basin petrogenesis is thus generated by interaction between the ''dry side'' and the ''wet side'' of the melting regime, which helps to account for the differences in behavior between back-arc and open ocean ridges.

[90] **Acknowledgments.** This work benefited from the very thorough reviews by Terry Plank and an anonymous reviewer and from discussions with Steve Parman and Paul Hall. We would like to thank Sue Woods for assistance on ICP-MS at Harvard University and Nilanjan Chatterjee and Steve Parman for assistance on electron Microprobe at the MIT Electron Microprobe Facility. This work was supported by the National Science Foundation grant OCE-0242618.

References

Asimow, P. D., and C. H. Langmuir (2003), The importance of water to oceanic mantle melting regimes, *Nature*, *421*, 815–820, doi:10.1038/nature01429.

Baker, M. B., M. M. Hirschmann, M. S. Ghiorso, and E. M. Stolper (1995), Compositions of near solidus peridotite melts from experiments and thermodynamic calculations, *Nature*, *363*, 63–65.

Bender, J. F., C. H. Langmuir, and G. N. Hanson (1984), Petrogenesis of basalt glasses from the Tamayo region, East Pacific Rise, *J. Petrol.*, *25*, 213–254.

Bézos, A. (2003), Étude des éléments lithophiles et fortement sidérophiles (Pd, Pt, Ru et Ir) dans les basaltes des dorsales océaniques, Ph.D. thesis, 318 pp., Univ. Paris Diderot, Paris.

Blundy, J. D., J. A. C. Robinson, and B. J. Wood (1998), Heavy REE are compatible in clinopyroxene on the spinel lherzolite solidus, *Earth Planet. Sci. Lett.*, *160*, 493–504, doi:10.1016/S0012-821X(98)00106-X.

Carroll, M. R., and M. J. Rutherford (1988), Sulfur speciation in hydrous experimental glasses of varying oxidation state: Results from measured wavelength shifts of sulfur X-rays, *Am. Mineral.*, *73*, 845–849.

Danyushevsky, L. V. (2001), The effect of small amounts of H_2O crystallization of mid-ocean ridge and backarc basin magmas, *J. Volcanol. Geotherm. Res.*, *110*, 265–280, doi:10.1016/S0377-0273(01)00213-X.

Danyushevsky, L. V., T. J. Falloon, A. V. Sobolev, A. J. Crawford, M. Carroll, and R. C. Price (1993), The H_2O content of basalt glasses from southwest Pacific back-arc basins, *Earth Planet. Sci. Lett.*, *117*, 347–362, doi:10.1016/0012-821X(93)90089-R.

Davies, J. H., and D. J. Stevenson (1992), Physical model of source region of subduction zone volcanics, *J. Geophys. Res.*, *97*, 2037–2070, doi:10.1029/91JB02571.

Donnelly, K. E., S. L. Goldstein, C. H. Langmuir, and M. Spiegelman (2004), Origin of enriched ocean ridge basalts and implications for mantle dynamics, *Earth Planet. Sci. Lett.*, *226*, 347–366, doi:10.1016/j.epsl.2004.07.019.

Edmonds, H. N., C. R. German, J. A. Breier, D. P. Connelly, A. Townsend-Small, J. A. Resing, C. Aumack, E. T. Baker, and C. H. Langmuir (2004), Plume mapping and shipboard chemical data used to locate new vent sites in the Lau Basin, *Eos Trans. AGU*, *85*(47), Fall Meet. Suppl., Abstract B13A–0191.

Eiler, J. M. (2001), Oxygen isotope variations of basaltic lavas and upper mantle rocks, in *Stable Isotope Geochemistry*, *Rev. Mineral.*, vol. 43, edited by J. W. Valley and D. R. Cole, pp. 319–364, Mineral. Soc. of Am., Washington, D.C.

Eiler, J. M., P. Schiano, J. W. Valley, N. T. Kita, and E. M. Stolper (2007), Oxygen-isotope and trace element constraints on the origins of silica-rich melts in the subarc mantle, *Geochem. Geophys. Geosyst.*, *8*, Q09012, doi:10.1029/2006GC001503.

Elliott, T., T. Plank, A. Zindler, W. White, and B. Bourdon (1997), Element transport from slab to volcanic front at the Mariana arc, *J. Geophys. Res.*, *102*, 14,991–15,019, doi:10.1029/97JB00788.

Ewart, A., K. D. Collerson, M. Regelous, J. I. Wendt, and Y. Niu (1998), Geochemical evolution within the Tonga-Kermadec Lau arc back-arc systems: The role of varying mantle wedge composition in space and time, *J. Petrol.*, *39*, 331–368, doi:10.1093/petrology/39.3.331.

Fornari, D. J. (2003), A new deep-sea towed digital camera and multi-rock coring system, *Eos Trans. AGU*, *84*(8), 69–76.

Gaetani, G. A., and T. L. Grove (2004), Experimental constraints on melt generation in the mantle wedge, in *Inside the Subduction Factory*, *Geophys. Monogr. Ser.*, vol. 138, edited by J. M. Eiler, pp. 107–134, AGU, Washington, D.C.

Garcia, M. O., N. W. K. Liu, and D. W. Muenow (1979), Volatiles in submarine volcanic rocks from the Mariana Island Arc and Trough, *Geochim. Cosmochim. Acta*, *43*, 305–312, doi:10.1016/0016-7037(79)90196-0.

Ghiorso, M. S., M. M. Hirschmann, P. W. Reiners, and V. C. Kress III (2002), The pMELTS: A revision of MELTS for improved calculation of phase relations and major element partitioning related to partial melting of the mantle to 3 GPa, *Geochem. Geophys. Geosyst.*, *3*(5), 1030, doi:10.1029/2001GC000217.

Gill, J. B. (1976), Composition and age of Lau Basin and ridge volcanic-rocks: Implications for evolution of an interarc basin and remnant arc, *Geol. Soc. Am. Bull.*, *87*, 1384–1395, doi:10.1130/0016-7606(1976)87<1384:CAAOLB>2.0.CO;2.

Gill, J. B. (1981), *Orogenic Andesites and Plate Tectonics*, 390 pp., Springer, New York.

Hall, P. S., and C. Kincaid (2001), Diapiric flow at subduction zones: A recipe for rapid transport, *Science*, *292*, 2472–2475, doi:10.1126/science.1060488.

Hawkins, J. W. (1995), Evolution of the Lau Basin: Insights from ODP leg 135, in *Active Margins and Marginal Basins of the Western Pacific*, *Geophys. Monogr. Ser.*, vol. 88, edited by B. Taylor and J. Natland, pp. 125–173, AGU, Washington, D.C.

Hergt, J. M., and J. D. Woodhead (2007), A critical evaluation of recent models for Lau-Tonga arc-backarc basin magmatic evolution, *Chem. Geol.*, *245*, 9–44, doi:10.1016/j.chemgeo.2007.07.022.

Hirschmann, M. M., P. D. Asimow, M. S. Ghiorso, and E. M. Stolper (1999), Calculation of peridotite partial melting from thermodynamic models of minerals and melts. III. Controls on isobaric melt production and the effect of water on melt production, *J. Petrol.*, *40*, 831–851, doi:10.1093/petrology/40.5.831.

Hofmann, A. W., and M. D. Feigenson (1983), Case studies on the origin of basalt, I. Theory and reassessment of Grenada basalts, *Contrib. Mineral. Petrol.*, *84*, 382–389, doi:10.1007/BF01160289.

Johnson, M. C., and T. Plank (1999), Dehydration and melting experiments constrain the fate of subducted sediments, *Geochem. Geophys. Geosyst.*, *1*(12), 1007, doi:10.1029/1999GC000014.

Kelley, K. A., and E. H. Hauri (2007), The composition of water-rich components in the sources of back-arc and arc magmas, *Eos Trans. AGU*, *88*(52), Fall Meet. Suppl., Abstract V52A–05.

Kelley, K. A., T. Plank, J. Ludden, and H. Staudigel (2003), Composition of altered oceanic crust at ODP Sites 801 and 1149, *Geochem. Geophys. Geosyst.*, *4*(6), 8910, doi:10.1029/2002GC000435.

Kelley, K. A., T. Plank, T. L. Grove, E. M. Stolper, S. Newman, and E. Hauri (2006), Mantle melting as a function of water content beneath back-arc basins, *J. Geophys. Res.*, *111*, B09208, doi:10.1029/2005JB003732.

Kent, A. J. R., D. W. Peate, S. Newman, E. M. Stolper, and J. A. Pearce (2002), Chlorine in submarine glasses from the Lau Basin: Seawater contamination and constraints on the composition of slab-derived fluids, *Earth Planet. Sci. Lett.*, *202*, 361–377, doi:10.1016/S0012-821X(02)00786-0.

Kessel, R., M. W. Schmidt, P. Ulmer, and T. Pettke (2005), Trace element signature of subduction-zone fluids, melts and supercritical liquids at 120–180km depth, *Nature*, *437*, 724–727, doi:10.1038/nature03971.

Klein, E. M., and C. H. Langmuir (1987), Global correlations of ocean ridge basalt chemistry with axial depth and crustal thickness, *J. Geophys. Res.*, *92*, 8089–8115, doi:10.1029/JB092iB08p08089.

Langmuir, C. H., E. M. Klein, and T. Plank (1992), Petrological systematics of mid-ocean ridge basalts: Constraints on melt generation beneath ocean ridges, in *Mantle Flow and Melt Generation at Mid-Ocean Ridges*, *Geophys. Monogr. Ser.*, vol. 71, edited by J. Phipps Morgan et al., pp. 183–280, AGU, Washington, D.C.

Langmuir, C. H., A. Bézos, S. Escrig, and S. W. Parman (2006), Chemical systematics and hydrous melting of the mantle in back-arc basins, in *Back-Arc Spreading Systems: Geological, Biological, Chemical, and Physical Interactions*, *Geophys. Monogr. Ser.*, vol. 166, edited by D. M. Christie et al., pp. 87–146, AGU, Washington, D. C.

Martinez, F., and B. Taylor (2002), Mantle wedge control on back-arc crustal accretion, *Nature*, *416*, 417–420.

Martinez, F., B. Taylor, E. T. Baker, J. A. Reising, and S. L. Walker (2006), Opposing trends in crustal thickness and spreading rate along the back-arc Eastern Lau Spreading Center: Implications for controls on ridge morphology, faulting and hydrothermal activity, *Earth Planet. Sci. Lett.*, *245*, 655–672, doi:10.1016/j.epsl.2006.03.049.

Mathez, E. (1976), Sulfur solubility and magmatic sulfides in submarine basalts glass, *J. Geophys. Res.*, *81*, 4269–4276, doi:10.1029/JB081i023p04269.

McCulloch, F. T., and J. A. Gamble (1991), Geochemical and geodynamical constraints on subduction zone magmatism, *Earth Planet. Sci. Lett.*, *102*, 358–374, doi:10.1016/0012-821X(91)90029-H.

McDade, P., J. D. Blundy, and B. J. Wood (2003), Trace element partitioning between mantle wedge peridotite and hydrous MgO-rich melt, *Am. Mineral.*, *88*, 1825–1831.

Michael, P. J., and R. L. Chase (1987), The influence of primary magma composition, H_2O and pressure on mid ocean ridge basalt differentiation, *Contrib. Mineral. Petrol.*, *96*, 245–263, doi:10.1007/BF00375237.

Michael, P. J., and W. C. Cornell (1998), Influence of spreading rate and magma supply on crystallization and assimilation beneath mid-ocean ridges: Evidence from chlorine and major element chemistry of mid-ocean ridge basalts, *J. Geophys. Res.*, *103*, 18,325–18,356.

Miller, D. M., S. L. Goldstein, and C. H. Langmuir (1994), Cerium/lead and lead-isotope ratios in arc magmas and the enrichment of lead in the continents, *Nature*, *368*, 514–520, doi:10.1038/368514a0.

Minster, J.-F., and C.-J. Allègre (1977), Systematic use of trace elements in igneous processes. Part III: Inverse problem of fractional crystallization in volcanic suites, *Contrib. Mineral. Petrol.*, *61*, 49–77, doi:10.1007/BF00375945.

Muenow, D. W., N. W. K. Liu, M. O. Garcia, and A. D. Saunders (1980), Volatiles in submarine volcanic-rocks from the spreading axis of the East Scotia sea back-arc basin, *Earth Planet. Sci. Lett.*, *47*, 272–278, doi:10.1016/0012-821X(80)90043-6.

Muenow, D. W., M. R. Perfit, and K. E. Aggrey (1991), Abundances of volatiles and genetic relationships among submarine basalts from the Woodlark basin, southwest Pacific, *Geochim. Cosmochim. Acta*, *55*, 2231–2239, doi:10.1016/0016-7037(91)90099-Q.

Nilsson, K., and C. Peach (1993), Sulfur speciation, oxidation state, and sulfur concentration in backarc magmas, *Geochim. Cosmochim. Acta*, *57*, 3807–3813, doi:10.1016/0016-7037(93)90158-S.

Pearce, J. A. (1994), Geochemistry of Lau Basin volcanic rocks: Influence of ridge segmentation and arc proximity, *Spec. Publ. Geol. Soc. London*, *81*, 53–75, doi:10.1144/GSL.SP.1994.081.01.04.

Pearce, J. A., and R. J. Stern (2006), The origin of back-arc basin magmas: Trace element and isotope perspectives, in *Back-Arc Spreading Systems: Geological, Biological, Chemical and Physical Interactions*, *Geophysical Monogr. Ser.*, vol. 166, edited by D. M. Christie et al., pp. 63–86, AGU, Washington, D. C.

Pearce, J. A., P. E. Baker, P. K. Harvey, and I. W. Luff (1995), Geochemical evidence for subduction fluxes, mantle melting and fractional crystallization beneath the south Sandwich island arc, *J. Petrol.*, *36*, 1073–1109.

Pearce, J. A., R. J. Stern, S. H. Bloomer, and P. Fryer (2005), Geochemical mapping of the Mariana arc-basin system: Implications for the nature and distribution of subduction components, *Geochem. Geophys. Geosyst.*, *6*, Q07006, doi:10.1029/2004GC000895.

Peate, D. W., T. F. Kokfelt, C. J. Hawkesworth, P. W. Van Calsteren, J. M. Hergt, and J. A. Pearce (2001), U-series isotope data on Lau Basin glasses: The role of subduction-related fluids during melt generation in back-arc basins, *J. Petrol.*, *42*, 1449–1470, doi:10.1093/petrology/42.8.1449.

Plank, T., and C. H. Langmuir (1998), The chemical composition of subducting sediments and its consequences for the crust and mantle, *Chem. Geol.*, *145*, 325–394, doi:10.1016/S0009-2541(97)00150-2.

Salters, V. J. M., and A. Stracke (2004), Composition of the depleted mantle, *Geochem. Geophys. Geosyst.*, *5*, Q05B07, doi:10.1029/2003GC000597.

Schmidt, M. W., and S. Poli (1998), Experimentally based water budgets for dehydrating slabs and consequences for arc magma generation, *Earth Planet. Sci. Lett.*, *163*, 361–379.

Sinton, J. M., and P. Fryer (1987), Mariana Trough lavas from 18°N: Implications for the origin of back arc basin basalts, *J. Geophys. Res.*, *92*, 12,782–12,802, doi:10.1029/JB092iB12p12782.

Sinton, J. M., L. L. Ford, B. Chappell, and M. T. McCulloch (2003), Magma genesis and mantle heterogeneity in the Manus back-arc basin, Papua New Guinea, *J. Petrol.*, *44*, 159–195, doi:10.1093/petrology/44.1.159.

Spiegelman, M., and P. B. Kelemen (2003), Extreme chemical variability as a consequence of channelized melt transport, *Geochem. Geophys. Geosyst.*, *4*(7), 1055, doi:10.1029/2002GC000336.

Stolper, E., and S. Newman (1994), The role of water in the petrogenesis of Mariana Trough magmas, *Earth Planet. Sci. Lett.*, *121*, 293–325, doi:10.1016/0012-821X(94)90074-4.

Sun, S. S., and W. F. McDonough (1989), Chemical and isotopic systematics of oceanic basalts: Implication for mantle composition and processes, in *Magmatism in Ocean Basins*, edited by A. D. Saunders and M. J. Norry, *Geol. Soc. Spec. Publ.*, vol. 42, pp. 313–345.

Taylor, B., and F. Martinez (2003), Back-arc basin basalt systematics, *Earth Planet. Sci. Lett.*, *210*, 481–497, doi:10.1016/S0012-821X(03)00167-5.

Taylor, B., K. Zellmer, F. Martinez, and A. Goodlife (1996), Sea-floor spreading in the Lau back-arc basin, *Earth Planet. Sci. Lett.*, *144*, 35–40, doi:10.1016/0012-821X(96)00148-3.

Tenthorey, E., and J. Hermann (2004), Composition of fluids during serpentinite breakdown in subduction zones: Evidence for limited boron mobility, *Geology*, *32*, 865–868, doi:10.1130/G20610.1.

Turner, S. P., and C. J. Hawkesworth (1998), Using geochemistry to map mantle flow beneath the Lau Basin, *Geology*, *26*, 1019–1022, doi:10.1130/0091-7613(1998)026<1019:UGTMMF>2.3.CO;2.

Turner, S., C. J. Hawkesworth, N. Rogers, J. Bartlett, T. Worthington, J. M. Hergt, J. A. Pearce, and I. Smith (1997), ^{238}U-^{230}Th disequilibria, magma petrogenesis, and flux rates beneath the depleted Tonga-Kermadec island arc, *Geochim. Cosmochim. Acta*, *61*, 4855–4884, doi:10.1016/S0016-7037(97)00281-0.

Wallace, P., and I. S. E. Carmichael (1992), Sulfur in basaltic magmas, *Geochim. Cosmochim. Acta*, *56*, 1863–1874, doi:10.1016/0016-7037(92)90316-B.

Weaver, J., and C. H. Langmuir (1990), Calculation of phase equilibrium in mineral-melt systems, *Comput. Geosci.*, *16*, 1–19, doi:10.1016/0098-3004(90)90074-4.

Wiens, D. A., K. A. Kelley, and T. Plank (2006), Mantle temperature variations beneath back-arc spreading centers inferred from seismology, petrology, and bathymetry, *Earth Planet. Sci. Lett.*, *248*, 16–27, doi:10.1016/j.epsl.2006.04.011.

Workman, R. K., S. R. Hart, M. Jackson, M. Regelous, K. A. Farley, J. Blusztajn, M. Kurz, and H. Staudigel (2004), Recycled metasomatized lithosphere as the origin of the Enriched Mantle II (EM2) end-member: Evidence from the Samoan Volcanic Chain, *Geochem. Geophys. Geosyst.*, *5*, Q04008, doi:10.1029/2003GC000623.

Workman, R. K., and S. R. Hart (2005), Major and trace element composition of the depleted MORB mantle (DMM), *Earth Planet. Sci. Lett.*, *231*, 53–72, doi:10.1016/j.epsl.2004.12.005.

P. D. Asimow, Division of Geological and Planetary Sciences, California Institute of Technology, Pasadena, CA 91125, USA.

A. Bézos, Laboratoire de Planetologie et Geodynamique de Nantes, UMR 6112, Université de Nantes, CNRS, F-44322 Nantes, France. (antoine.bezos@univ-nantes.fr)

S. Escrig and C. H. Langmuir, Department of Earth and Planetary Sciences, Harvard University, Cambridge, MA 02139, USA.

P. J. Michael, Department of Geosciences, University of Tulsa, Tulsa, OK 74014, USA.